Postprint of: Lewandowski-Szewczyk M.J., Stupkiewicz S., Non-standard contact conditions in generalized continua: microblock contact model for a Cosserat body, International Journal of Solids and Structures, 2020, https://doi.org/10.1016/j.ijsolstr.2020.07.001

Non-standard contact conditions in generalized continua: microblock contact model for a Cosserat body*

M.J. Lewandowski-Szewczyk[1,2] and S. Stupkiewicz[2,†]

[1] *Faculty of Civil and Environmental Engineering, Gdańsk University of Technology, 80-952 Gdańsk, Poland*
[2] *Institute of Fundamental Technological Research, Polish Academy of Sciences, Pawińskiego 5b, 02-106 Warsaw, Poland*

July 16, 2020

Abstract

Generalized continuum theories involve non-standard boundary conditions that are associated with the additional kinematic variables introduced in those theories, e.g., higher gradients of the displacement field or additional kinematic degrees of freedom. Accordingly, formulation of a contact problem for such a continuum necessarily requires that adequate contact conditions are formulated for the additional kinematic variables and/or for the respective generalized tractions. In this paper, we address several related open problems, namely, how to enhance the classic contact conditions to include the effects of the additional kinematic variables, how to link the enhanced contact model to the underlying microstructure of the solid, and how to do it in a consistent manner. As a first step towards a new class of contact models for generalized continua, a microblock contact model is derived for a Cosserat solid based on simple micromechanical considerations. To illustrate the non-trivial effects introduced by the non-standard boundary conditions, the problem of compression of an infinite strip with nonaligned microblocks is considered, and the analytical solution is derived for the corresponding boundary layers. A Hertz-like contact problem is also solved numerically with the focus on non-standard features of the solution and on the related size effects.

Keywords: microstructure; contact problems; size effects; boundary layers; Cosserat continuum

1 Introduction

Microstructured materials may exhibit size effects when the characteristic dimension of the body is sufficiently small compared to the characteristic size of the microstructure. However, the classic continuum theory is not capable of predicting those effects as it possesses no intrinsic length. One of the feasible approaches to modelling of the size effects is to resort to generalized continuum theories that include higher gradients of the displacement field, as in strain-gradient media (e.g. Koiter, 1964; Mindlin, 1965), gradients of internal variables, as in gradient

*Published in *Int. J. Solids Struct.*, 2020, doi: 10.1016/j.ijsolstr.2020.07.001
†Corresponding author, email: sstupkie@ippt.pan.pl

plasticity (e.g. Mühlhaus and Alfantis, 1991; Gurtin, 2000; Gao and Huang, 2001), or additional kinematic degrees of freedom, as in Cosserat or micromorphic theories (e.g. Cosserat and Cosserat, 1909; Nowacki, 1972; Eringen, 1968).

A common feature of the generalized continuum theories is that they necessarily involve non-standard boundary conditions in addition to the usual boundary conditions of the classic continuum, the latter constraining the displacements and surface tractions. For instance, the Cosserat continuum, specifically considered in this work, involves the boundary conditions that can be imposed on the microrotation, which is the additional kinematic degree of freedom, and on the micromoment, which is the generalized traction conjugate to the microrotation.

The importance of the additional boundary conditions emerges, in particular, in contact problems, for instance, in micro- and nano-indentation, in which size effects can be observed experimentally. Formulation of a related boundary value problem requires that adequate boundary conditions are specified on the contact surface. The main issue here is that application of a generalized continuum model implies that the contact conditions involve not only the displacements and surface tractions, as in the classic continuum, but also the additional boundary conditions that are related to the additional unknowns or gradient terms. The simplest choice is to assume that the respective generalized tractions are equal to zero (and this is a common choice, as discussed in more detail below), but this choice is not necessarily justified from the physical point of view.

The main problem that is addressed in this work is thus how to extend the classic contact conditions to include the effects of the additional variables characteristic for the generalized continuum at hand. Secondly, the question is how to relate the enhanced contact model to the underlying microstructure of the solid and how to ensure that the classic and non-standard contact variables involved in the enhanced model are coupled in a consistent manner. For instance, if the microstructured solid is elastic, then the resulting contact response is also expected to be elastic-like and thus to preserve the potential structure of the problem, in particular, to be free of any dissipative effects. Clearly, such consistency requirements impose restrictions on the desired enhanced contact model.

To the best of our knowledge, none of the issues mentioned above has been addressed in the literature to date. As a contribution towards filling this gap, a microblock contact model is derived in this work for a Cosserat solid, starting from simple micromechanical considerations. We focus on the Cosserat continuum because the additional degrees of freedom in this model have a clear physical interpretation and can be directly related to the rotations of the microstructural elements.

The Cosserat model is one of the simplest among the generalized continuum models. In their pioneering work, Cosserat and Cosserat (1909) postulated existence of additional rotational degrees of freedom apart from the classic translational ones. In fact, microstructural interpretation of this model states that at every material point a rigid triad or microblock subsists that can rotate, and this rotation (microrotation) is different from the macroscopic rotation (macrorotation) of the infinitesimal neighbourhood of the considered material point. When the microrotation is fully coupled to the macrorotation, the additional degrees of freedom are redundant, and the Cosserat model becomes the couple-stress model (Mindlin and Tiersten, 1962).

In the last century, the Cosserat model was used in numerous fields of mechanics with two main application reas. Firstly, the Cosserat model can be used as a framework for describing the underlying microstructure of the nalyzed material, for instance, for bone structures (Yang and Lakes, 1981; Lakes, 1995), cellular solids (Hård af egerstad et al., 2009; Spadoni and Ruzzene, 2012; Liu et al., 2012), and masonry structures (Masiani et al.,

1995; Sulem and Mühlhaus, 1997; Cerrolaza et al., 1999; Casolo, 2006). Secondly, the Cosserat continuum can be employed to regularize ill-posed problems thanks to the length-scale parameter introduced. Representative examples include damage plasticity (Steinmann, 1995; Addessi, 2014), singularities at the crack tip (Nakamura and Lakes, 1988; Forest et al., 2001), and shear banding in granular media (Vardoulakis, 1989; Tejchman and Bauer, 1996; Tejchman, 2008).

Contact problems for elastic generalized continua have attracted a limited attention to date. Semi-analytical solutions for selected contact problems in couple-stress elasticity have been obtained by Zisis et al. (2014) and Gourgiotis et al. (2016, 2019). Additional effects have also been included within the framework of couple-stress elasticity considering, e.g., friction (Wang et al., 2018), adhesion (Li and Liu, 2019), and piezoelectricity (Song et al., 2020). Garg et al. (2016) have used the finite-element method to study the indentation size effect in couple-stress elasticity with application to polymeric materials. Note that, in all cases mentioned above, homogeneous boundary conditions have been adopted for the higher-order tractions.

The indentation size effect in plasticity has been the subject of intense work for the last two decades (e.g. Nix and Gao, 1998; Pharr et al., 2010). Representative examples of finite-element simulations of the indentation problem include those employing isotropic gradient plasticity (Shu and Fleck, 1998; Huang et al., 2000, 2006; Wei and Hutchinson, 2003; Swaddiwudhipong et al., 2005; Qu et al., 2006) and gradient crystal plasticity (Lee and Chen, 2010; Reuber et al., 2014; Gao et al., 2015; Stupkiewicz and Petryk, 2016; Lewandowski and Stupkiewicz, 2018). Again, in all cases, the related finite-element computations use the standard contact conditions, sometimes accompanied by the so-called 'microclamped' boundary conditions for the plastic strain (or a related variable) prescribed on the contact surface (e.g. Shu and Fleck, 1998; Wei and Hutchinson, 2003), as an alternative to the more common 'microfree' boundary condition of vanishing generalized traction.

To the best of our knowledge, the only attempt to enhance the classic contact conditions for a generalized continuum is the work of Zhang et al. (2005). In the context of the elastic Cosserat continuum, it has been proposed that the increment of the micromoment at the contact interface is proportional to the increment of the relative microrotation at the interface with the proportionality coefficient depending on the normal contact pressure. The formulation proposed does not exhibit the potential structure that has been discussed earlier since the microrotations and micromoments do not influence the impenetrability condition formulated in the standard manner for the normal gap and contact pressure. Anyway, in the actual computations, the proposed enhancement was not used, and the common boundary condition of the vanishing micromoment were applied.

In the microblock contact model proposed in the present paper, the coupling between the displacements and microrotations at the contact interface results from simple micromechanical considerations, and the model exhibits the desired potential structure. The resulting enhanced contact model is apparently the first model of this kind.

The paper is organized as follows. In Section 2, the basic kinematic and constitutive equations for the linear elastic Cosserat model are recalled and the notation used throughout the paper is established. The microblock contact model in a 2D setting is developed in Section 3 along with the penalty and augmented Lagrangian treatment of the contact constraints. In Section 4, two sample contact problems are analyzed in order to illustrate the qualitative features introduced by the proposed contact model. Compression of an infinite strip with initially misaligned microblocks is studied first, and the analytical solution, which exhibits boundary layers, is found for this problem. A Hertz-like contact problem is also solved using the finite-element method. The related size effects

are examined, and the emerging boundary layers at the contact interface are discussed.

Notation

The following notation is used for vector and tensor operations (in orthonormal basis):

$$\begin{array}{ll} \mathbf{a} = \mathbf{B}\mathbf{c} & a_i = B_{ij}c_j \\ \mathbf{A} = \mathbf{B}\mathbf{C} & A_{ik} = B_{ij}C_{jk} \\ a = \mathbf{B} \cdot \mathbf{C} & a = B_{ij}C_{ji} \\ \mathbf{A} = \nabla\mathbf{a} & A_{ij} = a_{i,j} \\ [\mathbf{a}] = -\boldsymbol{\epsilon}\,\mathbf{a} & [a]_{ik} = -\epsilon_{ikm}a_m \\ \mathbf{a} = \boldsymbol{\epsilon} : \mathbf{A} & a_i = \epsilon_{ijk}A_{kj}, \end{array}$$

where $\boldsymbol{\epsilon}$ is the Levi-Civita pseudo-tensor, of which both the second- and third-order versions are used in this paper. For a second order tensor $\mathbf{A}$, the superscripts $\mathbf{A}^{\mathrm{sym}}$ and $\mathbf{A}^{\mathrm{skw}}$ denote the symmetric and skew-symmetric part of the tensor, respectively, $A_{ij}^{\mathrm{sym}} = \frac{1}{2}\left(A_{ij} + A_{ji}\right)$, $A_{ij}^{\mathrm{skw}} = \frac{1}{2}\left(A_{ij} - A_{ji}\right)$.

2 Basic equations of the Cosserat continuum

2.1 Kinematics

The Cosserat continuum involves an additional, independent kinematic degree of freedom, in addition to the usual displacement field $\mathbf{u}$ (Cosserat and Cosserat, 1909). This new variable, denoted by $\boldsymbol{\psi}$, is a vector of infinitesimal rotations. From many available notations describing the kinematics, we follow the one used, e.g., by Cerrolaza et al. (1999); Vardoulakis (2019). The so-called relative deformation measure $\boldsymbol{\gamma}$ is introduced in the following form,

$$\boldsymbol{\gamma} = \nabla\mathbf{u} + \boldsymbol{\epsilon}\,\boldsymbol{\psi}. \tag{1}$$

The symmetric part of $\boldsymbol{\gamma}$ restores the strain tensor of the classic continuum,

$$\boldsymbol{\gamma}^{\mathrm{sym}} = \boldsymbol{\varepsilon} = (\nabla\mathbf{u})^{\mathrm{sym}}. \tag{2}$$

The skew-symmetric part of $\boldsymbol{\gamma}$ describes the infinitesimal relative rotation at the Cosserat continuum point,

$$\boldsymbol{\gamma}^{\mathrm{skw}} = \boldsymbol{\omega} + \boldsymbol{\epsilon}\,\boldsymbol{\psi}, \tag{3}$$

where $\boldsymbol{\omega} = (\nabla\mathbf{u})^{\mathrm{skw}}$. The tensor of infinitesimal rotation $\boldsymbol{\omega}$ can be expressed as an axial rotation vector,

$$\mathbf{r} = \frac{1}{2}\boldsymbol{\epsilon} : \boldsymbol{\omega}. \tag{4}$$

The inverse transformation also holds, $\boldsymbol{\omega} = -\boldsymbol{\epsilon}\,\mathbf{r}$. The infinitesimal microrotation vector $\boldsymbol{\psi}$, represented by a second-order tensor, is defined as

$$[\boldsymbol{\psi}] = -\boldsymbol{\epsilon}\,\boldsymbol{\psi}. \tag{5}$$

Thus, the skew-symmetric part of the relative deformation measure $\boldsymbol{\gamma}$ denotes the difference between the infinitesimal rotation of the neighboring points and the Cosserat microrotation,

$$\boldsymbol{\gamma}^{\mathrm{skw}} = -\boldsymbol{\epsilon}\,(\mathbf{r} - \boldsymbol{\psi}) = \boldsymbol{\omega} - [\boldsymbol{\psi}]. \tag{6}$$

The last measure of deformation is related to the change of the microrotation $\boldsymbol{\psi}$ from point to point of the continuum. The quantity describing these changes is the gradient of the microrotation,

$$\boldsymbol{\kappa} = \nabla\boldsymbol{\psi}, \tag{7}$$

called the curvature tensor.

2.2 Linear elastic Cosserat model

Equilibrium of a linear elastic Cosserat solid that occupies domain Ω corresponds to the minimum of the potential energy functional Π,

$$\Pi[\mathbf{u}, \boldsymbol{\psi}] = \int_{\Omega} \left(W_{\mathrm{el}}(\boldsymbol{\gamma}, \boldsymbol{\kappa}) - \mathbf{f}\cdot\mathbf{u} - \mathbf{l}\cdot\boldsymbol{\psi}\right) \mathrm{d}V - \int_{\Gamma_{\mathrm{t}}} \mathbf{t}^{*}\cdot\mathbf{u}\,\mathrm{d}S - \int_{\Gamma_{\mathrm{M}}} \mathbf{M}^{*}\cdot\boldsymbol{\psi}\,\mathrm{d}S\,, \tag{8}$$

which leads to the following two-field minimization problem,

$$\min_{\mathbf{u},\boldsymbol{\psi}} \Pi[\mathbf{u}, \boldsymbol{\psi}]. \tag{9}$$

Here, Γ_{t} and Γ_{M} represent the parts of the boundary of Ω where, respectively, the traction vector $\mathbf{t}^{*}$ and the micromoment (couple stress) vector $\mathbf{M}^{*}$ are prescribed. In general, these two parts of the boundary may overlap or be distinct, which results in more combinations of boundary conditions than in the classic elasticity theory. Furthermore, $\mathbf{f}$ and $\mathbf{l}$ denote the body force and body micromoment, respectively.

The elastic strain energy of the linear isotropic Cosserat continuum comprises two parts,

$$W_{\mathrm{el}}(\boldsymbol{\gamma}, \boldsymbol{\kappa}) = W_{\gamma}(\boldsymbol{\gamma}) + W_{\kappa}(\boldsymbol{\kappa}). \tag{10}$$

The first part of the elastic strain is the classic continuum strain energy for the isotropic case with an additional coupling between non-local microrotations $\boldsymbol{\psi}$ and infinitesimal macrorotations $\boldsymbol{\omega}$,

$$W_{\gamma} = \frac{1}{2}\lambda\,(\operatorname{tr}\boldsymbol{\varepsilon})^2 + \mu\|\boldsymbol{\varepsilon}\|^2 + \mu_{\mathrm{c}}\left\|\boldsymbol{\gamma}^{\mathrm{skw}}\right\|^2, \tag{11}$$

where λ and μ are Lamé constants, and $\mu_{\mathrm{c}} \geq 0$ plays the role of a coupling modulus. When μ_{c} tends to infinity, we arrive at the couple-stress model, where there are no microrotations $\boldsymbol{\psi}$, since $[\boldsymbol{\psi}] = \boldsymbol{\omega}$. The curvature $\boldsymbol{\kappa}$ is then expressed via higher order derivatives of displacements, which has its consequences that are not discussed in this paper.

The second part of the elastic strain is the curvature energy that can be expressed in various forms; here we follow the notation used by Neff (2008),

$$W_{\kappa}(\boldsymbol{\kappa}) = \frac{1}{2}\ell^2\mu\left(\alpha'\,(\operatorname{tr}\boldsymbol{\kappa})^2 + (\gamma' + \beta')\|\boldsymbol{\kappa}^{\mathrm{sym}}\|^2 + (\gamma' - \beta')\left\|\boldsymbol{\kappa}^{\mathrm{skw}}\right\|^2\right), \tag{12}$$

with certain restrictions imposed on the material parameters to satisfy the ellipticity conditions (real wave speeds in wave propagation problems),

$$\lambda + \mu > 0, \qquad \mu_c + \mu > 0, \qquad \gamma' > 0, \qquad \alpha' + \beta' + \gamma' > 0, \tag{13}$$

as proved by Neff (2008). Neff et al. (2010) proposed a variant of the classic Cosserat model that satisfies weaker, so-called conformal curvature requirements. We do not consider this model, as we concentrate on the 2D setting of the Cosserat continuum, in which the curvature energy simplifies. In Eq. (12), ℓ is a material length-scale parameter of the Cosserat continuum.

The virtual work principle for the Cosserat continuum is obtained by rendering the variation of the potential energy (8) with respect to the fields of $\mathbf{u}$ and $\boldsymbol{\psi}$ equal to zero, $\delta\Pi = 0$, viz.

$$G[\mathbf{u}, \boldsymbol{\psi}; \delta\mathbf{u}, \delta\boldsymbol{\psi}] = \int_\Omega (\boldsymbol{\sigma} \cdot \delta\boldsymbol{\gamma} + \mathbf{m} \cdot \delta\boldsymbol{\psi} - \mathbf{f} \cdot \delta\mathbf{u} - \mathbf{l} \cdot \delta\boldsymbol{\psi}) \, \mathrm{d}V - \int_{\Gamma_\mathrm{t}} \mathbf{t}^* \cdot \delta\mathbf{u} \, \mathrm{d}S - \int_{\Gamma_\mathrm{M}} \mathbf{M}^* \cdot \delta\boldsymbol{\psi} \, \mathrm{d}S = 0 \qquad \forall \, \delta\mathbf{u}, \delta\boldsymbol{\psi}, \tag{14}$$

where $\delta\mathbf{u}$ and $\delta\boldsymbol{\psi}$ are the test functions (virtual displacements) such that

$$\delta\mathbf{u} = \mathbf{0} \quad \text{on } \Gamma_\mathrm{u} \quad \text{and} \quad \delta\boldsymbol{\psi} = \mathbf{0} \quad \text{on } \Gamma_\psi, \qquad \delta\boldsymbol{\gamma} = \nabla\delta\mathbf{u} + \boldsymbol{\epsilon}\,\delta\boldsymbol{\psi}, \tag{15}$$

and Γ_u and Γ_ψ are the parts of the boundary where, respectively, the displacements $\mathbf{u}$ and the microrotations $\boldsymbol{\psi}$ are prescribed. As in the case of Γ_t and Γ_M, the boundaries Γ_u and Γ_ψ may overlap or be distinct.

In the equations above, $\boldsymbol{\sigma}$ is a non-symmetric counterpart of Cauchy stress tensor in the classic continuum theory,

$$\boldsymbol{\sigma} = \lambda \, (\mathrm{tr}\,\boldsymbol{\gamma}) \, \mathbf{I} + 2\mu \, \boldsymbol{\gamma}^{\mathrm{sym}} + 2\mu_c \, \boldsymbol{\gamma}^{\mathrm{skw}}, \tag{16}$$

and $\mathbf{m}$ is the couple stress tensor,

$$\mathbf{m} = \ell^2 \mu \left(\alpha' \, (\mathrm{tr}\,\boldsymbol{\kappa}) \, \mathbf{I} + (\gamma' + \beta') \, \boldsymbol{\kappa}^{\mathrm{sym}} + (\gamma' - \beta') \, \boldsymbol{\kappa}^{\mathrm{skw}} \right). \tag{17}$$

In a 2D plane-strain setting, the first part of the elastic strain W_γ remains intact. However, all tensor quantities regarding the micromoments can be reduced by one order, which means that the infinitesimal microrotations vector $\boldsymbol{\psi}$ and the second-order curvature tensor $\boldsymbol{\kappa}$ reduce to a scalar $\psi = \psi_3$ and vector $\boldsymbol{\kappa} = \nabla\psi$, respectively. Thus, the second part of the elastic strain energy simplifies to

$$W_\kappa(\boldsymbol{\kappa}) = \frac{1}{2} \ell^2 \mu \|\boldsymbol{\kappa}\|^2, \tag{18}$$

which results in the following constitutive relation for the micromoment vector, $\mathbf{m} = \ell^2 \mu \boldsymbol{\kappa}$.

For the sake of completeness, we present the set of balance equations in the strong form,

$$\begin{aligned}
&\mathrm{div}\,\boldsymbol{\sigma} + \mathbf{f} = 0 && \text{in } \Omega, \\
&\mathrm{div}\,\mathbf{m} - \boldsymbol{\epsilon} : \boldsymbol{\sigma} + \mathbf{l} = 0 && \text{in } \Omega, \\
&\boldsymbol{\sigma}\,\mathbf{n} = \mathbf{t}^* && \text{on } \Gamma_\mathrm{t}, \\
&\mathbf{m}\,\mathbf{n} = \mathbf{M}^* && \text{on } \Gamma_\mathrm{M}, \\
&\mathbf{u} = \mathbf{u}^* && \text{on } \Gamma_\mathrm{u}, \\
&\boldsymbol{\psi} = \boldsymbol{\psi}^* && \text{on } \Gamma_\psi,
\end{aligned} \tag{19}$$

where $\mathbf{u}^*$ is the displacement prescribed on Γ_u, and $\boldsymbol{\psi}^*$ is the microrotation prescribed on Γ_ψ.

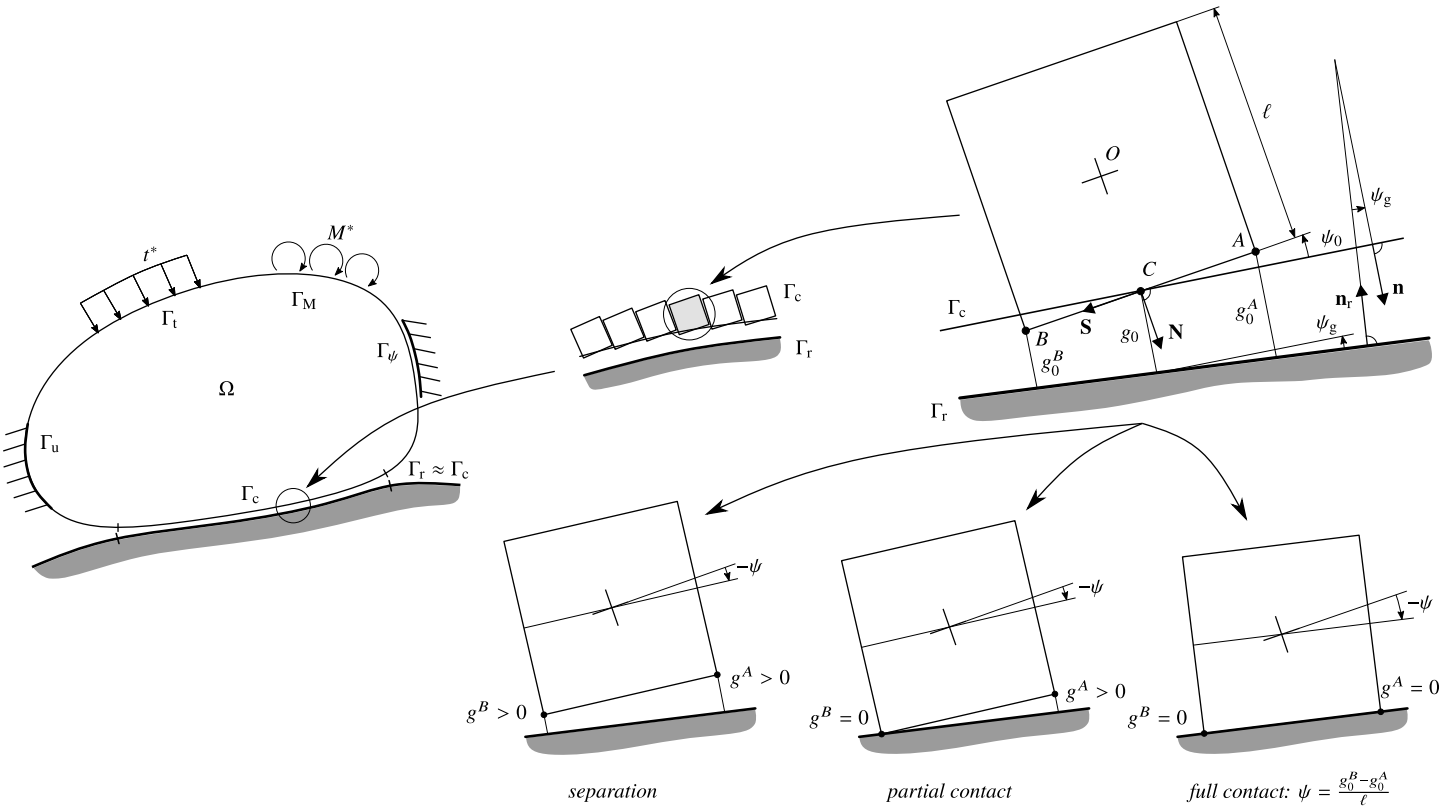

Figure 1: Microblock contact model.

3 Microblock contact model

3.1 Derivation of the model from micromechanical considerations

Consider frictionless contact of a Cosserat body with a rigid smooth obstacle represented by surface Γ_r with the unit outer normal $\mathbf{n}_r$. The potential contact surface of the body is denoted by Γ_c and $\mathbf{n}$ is the corresponding unit outer normal. In the context of contact mechanics, the usual assumptions of the small-strain kinematics imply that the two contacting surfaces coincide in space, $\Gamma_c \approx \Gamma_r$, and the two normal vectors are the opposite of each other, $\mathbf{n}_r \approx -\mathbf{n}$. Considering that $\Gamma_c \approx \Gamma_r$, the initial separation (or penetration) of the two surfaces is independently specified by the initial gap $g_0 = g_0(\mathbf{x})$ that is defined for each $\mathbf{x} \in \Gamma_c$. The considerations that follow are limited to 2D problems.

In order to account for the underlying microstructure of the Cosserat continuum, it is assumed that, at each point on the contact surface Γ_c, the contact interaction with the rigid obstacle occurs through a *rigid microblock*, and specifically through its two corners denoted by A and B, see Fig. 1. Accordingly, three contact states are possible: *separation*, when both corners are in separation; *partial contact*, when one corner is in separation and the other one is in contact; and *full contact*, when both corners are in contact.

Consider thus a typical contact point C on Γ_c with the position of C specified by $\mathbf{x} \in \Gamma_c$. The positions of the microblock centroid O and its two corners A and B are specified by

$$\mathbf{x}^O = \mathbf{x} - \frac{1}{2}\ell\,\mathbf{N}, \qquad \mathbf{x}^A = \mathbf{x}^O + \frac{1}{2}\ell(\mathbf{N} - \mathbf{S}), \qquad \mathbf{x}^B = \mathbf{x}^O + \frac{1}{2}\ell(\mathbf{N} + \mathbf{S}), \tag{20}$$

where ℓ is the length of the microblock side, assumed equal to the internal material length scale of the Cosserat continuum, while $\mathbf{N}$ and $\mathbf{S} = \mathbf{N} \times \mathbf{e}_3$ are, respectively, the unit normal and tangent to the microblock side, cf. Fig. 1. The microblocks can be initially rotated with respect to the contact surface, thus in general $\mathbf{N} \neq \mathbf{n}$, and this initial rotation is specified by a (small) angle ψ_0 that, in general, may depend on the position. The initial rotation may be interpreted as a kind of surface roughness since the contact interaction may then appear when there is separation between the nominal surfaces. Additionally, it leads to an asymmetry of the contact interaction due to the related contact micromoment. Both effects are illustrated in Section 4.

The (infinitesimal) translation and rotation of the microblock are specified by the displacement $\mathbf{u} = \mathbf{u}(\mathbf{x})$ and microrotation $\psi = \psi(\mathbf{x})$ of the contact point C. The displacements of the corners A and B are thus given by

$$\begin{aligned} \mathbf{u}^A &= \mathbf{u} + (\mathbf{I} + [\boldsymbol{\psi}])(\mathbf{x}^A - \mathbf{x}^O) - (\mathbf{x}^A - \mathbf{x}^O) = \mathbf{u} + \frac{1}{2}\ell\,[\boldsymbol{\psi}]\,(\mathbf{N} - \mathbf{S}) = \mathbf{u} - \frac{1}{2}\ell\,(\mathbf{S} + \mathbf{N})\,\psi, \\ \mathbf{u}^B &= \mathbf{u} + (\mathbf{I} + [\boldsymbol{\psi}])(\mathbf{x}^B - \mathbf{x}^O) - (\mathbf{x}^B - \mathbf{x}^O) = \mathbf{u} + \frac{1}{2}\ell\,[\boldsymbol{\psi}]\,(\mathbf{N} + \mathbf{S}) = \mathbf{u} - \frac{1}{2}\ell\,(\mathbf{S} - \mathbf{N})\,\psi, \end{aligned} \tag{21}$$

where $\mathbf{I} + [\boldsymbol{\psi}]$, such that $(\mathbf{I} + [\boldsymbol{\psi}])_{ij} = \delta_{ij} - \psi\epsilon_{ij}$, is the tensor of infinitesimal counterclockwise rotation by angle ψ around the z-axis, and ϵ_{ij} denotes the 2D counterpart of the Levi-Civita permutation pseudo-tensor.

As mentioned above, the contact conditions are checked for the two corners A and B. Accordingly, we define the normal gap for each corner,

$$g^\alpha = g_0^\alpha - \mathbf{u}^\alpha \cdot \mathbf{n}, \qquad \alpha = A, B, \tag{22}$$

where g_0^α denotes the initial gap at the corner α and is determined by contact geometry. Note that, in general, the initial gap g_0^α is not necessarily equal to the nominal initial gap g_0, which is defined for point C, thus $g_0^\alpha \neq g_0$, see the sketch in Fig. 1. The difference may stem from the initial microrotation ψ_0 and from the misalignment of the contacting surfaces Γ_c and Γ_r characterized by a (small) angle $\psi_\mathrm{g} \approx \sin(\psi_\mathrm{g}) = (\mathbf{n} \times \mathbf{n}_\mathrm{r}) \cdot \mathbf{e}_3$, see Fig. 1. In full contact, we have thus $\psi = -(\psi_0 + \psi_\mathrm{g})$.

The contact problem can now be formulated as a constrained minimization problem,

$$\min_{\mathbf{u},\psi} \Pi[\mathbf{u}, \psi] \quad \text{subject to } g^A \geq 0,\ g^B \geq 0 \text{ on } \Gamma_\mathrm{c}, \tag{23}$$

where g^A and g^B depend on $\mathbf{u}$ and ψ through Eqs. (22) and (21).

Following the standard approach (e.g., Nocedal and Wright, 2006), we introduce a Lagrangian functional,

$$\mathcal{L}[\mathbf{u}, \psi, \lambda^\alpha] = \Pi[\mathbf{u}, \psi] + \int_{\Gamma_\mathrm{c}} (\lambda^A g^A + \lambda^B g^B)\,\mathrm{d}S\,, \tag{24}$$

where λ^α are the Lagrange multipliers defined on Γ_c. At the solution of the constrained minimization problem (23), the Lagrangian $\mathcal{L}$ is stationary with respect to the variations of $\mathbf{u}$ and ψ, thus

$$G[\mathbf{u}, \psi; \delta\mathbf{u}, \delta\psi] + \int_{\Gamma_\mathrm{c}} (\lambda^A \delta g^A + \lambda^B \delta g^B)\,\mathrm{d}S = 0 \qquad \forall\, \delta\mathbf{u}, \delta\psi, \tag{25}$$

where G represents the variation of the potential energy Π, cf. Eq. (14), and the following complementarity conditions are satisfied,

$$\lambda^\alpha \leq 0, \qquad g^\alpha \geq 0, \qquad \lambda^\alpha g^\alpha = 0, \qquad \alpha = A, B. \tag{26}$$

The complementarity conditions (26) are recognized as the standard unilateral contact (Signorini) conditions, here formulated for both corners of the microblocks distributed along the contact surface Γ_c.

Using Eqs. (22) and (21), the variations of the normal gaps g^α are obtained in the following form,

$$\begin{aligned} \delta g^A &= -\delta\mathbf{u}\cdot\mathbf{n} + \frac{1}{2}\ell\,\mathbf{n}\cdot(\mathbf{S}+\mathbf{N})\,\delta\psi, \\ \delta g^B &= -\delta\mathbf{u}\cdot\mathbf{n} + \frac{1}{2}\ell\,\mathbf{n}\cdot(\mathbf{S}-\mathbf{N})\,\delta\psi, \end{aligned} \tag{27}$$

and the stationarity condition (25) can be expressed in the following form,

$$G[\mathbf{u},\psi;\delta\mathbf{u},\delta\psi] - \int_{\Gamma_c} (t_n\mathbf{n}\cdot\delta\mathbf{u} + M\,\delta\psi)\,\mathrm{d}S = 0 \qquad \forall\,\delta\mathbf{u},\delta\psi, \tag{28}$$

where

$$t_n = \lambda^A + \lambda^B, \qquad M = -\frac{1}{2}\ell\left(\mathbf{n}\cdot(\mathbf{S}+\mathbf{N})\,\lambda^A + \mathbf{n}\cdot(\mathbf{S}-\mathbf{N})\,\lambda^B\right). \tag{29}$$

It follows that $\mathbf{t} = t_n\mathbf{n}$ is the contact traction vector, t_n being its normal component (recall that frictionless contact is considered thus the tangential traction vanishes), while M is the contact micromoment, cf. the respective integrals over the boundaries Γ_t and Γ_M in the virtual work principle (14). Eq. (29) delivers also a physical interpretation of the Lagrange multipliers λ^α that contribute to the normal contact traction t_n and to the micromoment M, the latter being proportional to the microblock size ℓ.

3.2 Penalty formulation for a planar interface with aligned microblocks

To illustrate the features of the proposed microblock contact model, let us consider the special case of a planar contact interface with the microblocks aligned with the contact surface, thus $\psi_0 = 0$ and $\mathbf{N} = \mathbf{n}$. According to Eqs. (22) and (21), the normal gaps in this particular case have the following form,

$$g^A = g_0^A - \mathbf{u}\cdot\mathbf{n} + \frac{1}{2}\ell\psi, \qquad g^B = g_0^B - \mathbf{u}\cdot\mathbf{n} - \frac{1}{2}\ell\psi. \tag{30}$$

It follows that a positive microrotation ψ increases the gap at corner A and decreases the gap at corner B. At the same time, as in the usual contact formulations, a positive normal component of the displacement decreases the gap at both corners.

Upon introducing the standard penalty regularization of the inequality constraints $g^\alpha \geq 0$ (e.g., Wriggers, 2006), the constrained minimization problem (23) is transformed to the following unconstrained minimization problem,

$$\min_{\mathbf{u},\psi} \Pi^{\mathrm{pen}}[\mathbf{u},\psi], \qquad \Pi^{\mathrm{pen}}[\mathbf{u},\psi] = \Pi[\mathbf{u},\psi] + \int_{\Gamma_c} \frac{1}{2}\varrho\left(\langle g^A\rangle_-^2 + \langle g^B\rangle_-^2\right)\mathrm{d}S, \tag{31}$$

where the total penalty-regularized potential energy functional Π^{pen} includes now the contact contribution with $\varrho > 0$ denoting the penalty coefficient, and the following notation has been used,

$$\langle x\rangle_- = \begin{cases} x & \text{for } x \leq 0, \\ 0 & \text{for } x > 0. \end{cases} \tag{32}$$

As it is well known, the penalty parameter ϱ must be sufficiently high to avoid excessive violation of the impenetrability condition, while its excess value may lead to ill-conditioning of the contact problem (Wriggers, 2006).

The necessary condition for the minimum (31) is that Π^{pen} is stationary with respect to the variations of $\mathbf{u}$ and ψ, which leads to the virtual work principle in the form (28) with the normal contact traction t_{n} and contact micromoment M given by

$$t_{\text{n}} = t_{\text{n}}^A + t_{\text{n}}^B, \qquad M = \frac{1}{2}\ell(t_{\text{n}}^B - t_{\text{n}}^A), \qquad t_{\text{n}}^\alpha = \varrho\langle g^\alpha\rangle_-. \tag{33}$$

Let us examine the above expressions in more detail. In the case of full contact, i.e. $g^A < 0$ and $g^B < 0$, we have

$$t_{\text{n}} = 2\varrho\left(\frac{1}{2}(g_0^A + g_0^B) - \mathbf{u}\cdot\mathbf{n}\right), \qquad M = \frac{1}{2}\varrho\ell(g_0^B - g_0^A - \ell\psi). \tag{34}$$

It follows that the normal contact traction t_{n} depends only on the normal displacement and the contact micromoment M depends only on the microrotation ψ. The two contact laws are thus decoupled. We also note that the effective contact stiffness in the normal contact law is 2ϱ, and the respective effective initial gap is equal to the mean of the initial gaps g_0^A and g_0^B, cf. Eq. $(34)_1$.

In the case of partial contact, for instance, for $g^A < 0$ and $g^B > 0$, we have

$$t_{\text{n}} = \varrho\left(g_0^A - \mathbf{u}\cdot\mathbf{n} + \frac{1}{2}\ell\psi\right), \qquad M = -\frac{1}{2}\varrho\ell\left(g_0^A - \mathbf{u}\cdot\mathbf{n} + \frac{1}{2}\ell\psi\right), \tag{35}$$

so that a coupled contact law is obtained, in which both t_{n} and M depend on the displacement $\mathbf{u}$ and microrotation ψ. Furthermore, the following relationship holds,

$$\frac{\partial(t_{\text{n}}\mathbf{n})}{\partial\psi} = \frac{\partial M}{\partial\mathbf{u}} = \frac{1}{2}\varrho\ell\mathbf{n}, \tag{36}$$

and this symmetry reflects the potential structure of the contact law. Clearly, this symmetry relationship trivially holds also in the case of full contact when there is no coupling between the normal and micromoment contact interactions.

3.3 Augmented Lagrangian treatment of contact constraints

In the augmented Lagrangian method (Alart and Curnier, 1991), the constrained minimization problem (23) is transformed to an equivalent unconstrained saddle-point problem,

$$\min_{\mathbf{u},\psi}\max_{\lambda^\alpha}\mathcal{L}[\mathbf{u},\psi,\lambda^\alpha], \qquad \mathcal{L}[\mathbf{u},\psi,\lambda^\alpha] = \Pi[\mathbf{u},\psi] + \int_{\Gamma_{\text{c}}}\sum_\alpha L(g^\alpha,\lambda^\alpha)\,\mathrm{d}S\,, \tag{37}$$

where

$$L(g^\alpha,\lambda^\alpha) = \begin{cases}\left(\lambda^\alpha + \dfrac{\varrho}{2}g^\alpha\right)g^\alpha & \text{for } \hat\lambda^\alpha \le 0 \ \text{ (contact)},\\ -\dfrac{1}{2\varrho}\,(\lambda^\alpha)^2 & \text{for } \hat\lambda^\alpha > 0 \ \text{ (separation)},\end{cases} \tag{38}$$

and $\varrho > 0$ is a regularization parameter. Further, λ^α are the Lagrange multipliers defined on the contact surface Γ_c, and the augmented Lagrange multipliers $\hat{\lambda}^\alpha = \lambda^\alpha + \varrho g^\alpha$ are used to determine whether the contact state ($\hat{\lambda}^\alpha \leq 0$) or the separation state ($\hat{\lambda}^\alpha > 0$) occurs at the respective corners.

Note that function L defined by Eq. (38) is C^1-differentiable so that the necessary condition for the saddle point of $\mathcal{L}$ can be directly formulated as the condition of stationarity of $\mathcal{L}$ with respect to the variations of all its arguments. As a result, the following augmented virtual work principle is obtained,

$$G[\mathbf{u}, \psi; \delta\mathbf{u}, \delta\psi] + \int_{\Gamma_c} \sum_\alpha (\hat{\lambda}^\alpha_{\text{eff}} \delta g^\alpha + C^\alpha \delta\lambda^\alpha)\, \mathrm{d}S = 0 \qquad \forall\, \delta\mathbf{u}, \delta\psi, \delta\lambda^\alpha, \tag{39}$$

where the variations δg^α are given by (27), and

$$\hat{\lambda}^\alpha_{\text{eff}} = \frac{\partial L(g^\alpha, \lambda^\alpha)}{\partial g^\alpha} = \begin{cases} \hat{\lambda}^\alpha & \text{for } \hat{\lambda}^\alpha \leq 0, \\ 0 & \text{for } \hat{\lambda}^\alpha > 0, \end{cases} \qquad C^\alpha = \frac{\partial L(g^\alpha, \lambda^\alpha)}{\partial \lambda^\alpha} = \begin{cases} g^\alpha & \text{for } \hat{\lambda}^\alpha \leq 0, \\ -\dfrac{1}{\varrho}\lambda^\alpha & \text{for } \hat{\lambda}^\alpha > 0. \end{cases} \tag{40}$$

It follows that, in the augmented virtual work (39), the variation with respect to λ^α implies the condition $C^\alpha = 0$, which effectively enforces the constraints $g^\alpha = 0$ in the contact state and $\lambda^\alpha = 0$ in the separation state, in agreement with the complementarity conditions (26). The Lagrange multiplier λ^α represents the normal contact traction corresponding to the respective microblock corner. The split of the contribution of the normal contact traction to the parts acting on $\delta\mathbf{u}$ and on $\delta\psi$ arises from the variation δg^α of the normal gap according to Eq. (27).

As already mentioned, function L is C^1-differentiable, which guarantees continuity of both $\hat{\lambda}^\alpha_{\text{eff}}$ and C^α when the contact state changes. This allows one to efficiently solve the resulting set of equations, after introducing a spatial discretization, using the Newton method. The critical feature of the augmented Lagrangian approach is that contact conditions are satisfied precisely at the converged solution, and the regularization parameter ϱ does not affect the solution itself, possibly affecting the convergence of the iterative scheme, see e.g. Lengiewicz et al. (2011).

3.4 Finite-element implementation

In the present finite-element computations, four-noded quadrilateral elements with bilinear shape functions for both displacement and microrotation fields are used for the Cosserat continuum in 2D. This implies a piecewise-linear approximation of the two fields on the contact boundary. The contact constraints are then enforced at the nodes, which corresponds to the nodal (Lobatto) quadrature applied to the contact integral in the augmented virtual work (39). As required by the augmented Lagrangian method, two Lagrange multipliers are introduced as the additional global unknowns at each contact node to enforce the contact constraints (26) corresponding to the two microblock corners. The finite-element implementation and the computations have been performed using the *AceGen/AceFEM* package (Korelc, 2009; Korelc and Wriggers, 2016).

4 Illustrative examples

4.1 Infinite strip with nonaligned microblocks compressed by two rigid planes

In order to illustrate the features of the microblock contact model and the effects it introduces to the Cosserat continuum, an analytical solution is derived in this section for the problem of an infinite strip of thickness $2H$ compressed by two rigid planes. Non-trivial effects are introduced to the problem by assuming that the microblocks at the contact interfaces are initially rotated counterclockwise by a small angle ψ_0, see Fig. 2. Initially, the rigid planes are in contact with corners B, thus $g_0^B = 0$ and $g_0^A = \ell\psi_0$ along the interfaces, and hence there is a gap of $\frac{1}{2}\ell\psi_0$ between the rigid planes and the nominal contact surfaces. Loading is applied by prescribing the motion of the two rigid surfaces by δ towards the strip, cf. Fig. 2. The resulting problem is one-dimensional such that the unknown displacements and microrotations depend only on x_2. In particular, the assumption that the horizontal displacement depends only on x_2, thus $u_1 = u_1(x_2)$, implies that the strip is laterally constrained in the infinity, $x_1 \to \pm\infty$. It follows that the solution is symmetric with respect to $x_2 = 0$ such that $u_i(x_2) = -u_i(-x_2)$ and $\psi(x_2) = \psi(-x_2)$. Accordingly, it suffices to consider only the contact conditions at the upper contact surface $x_2 = H$.

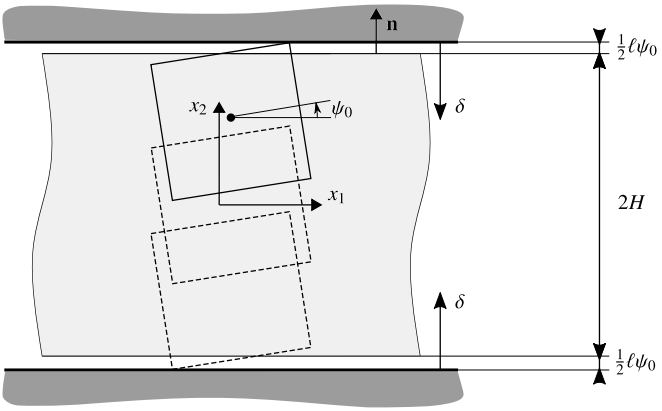

Figure 2: Infinite strip of elastic Cosserat material compressed by two rigid planes.

Since the initial rotation ψ_0 is small, the normal vector $\mathbf{N}$ is given as

$$\mathbf{N} = (-\sin\psi_0, \cos\psi_0) \approx (-\psi_0, 1), \tag{41}$$

and thus $\mathbf{S} \approx (1, \psi_0)$. Point B is in contact with the rigid plane during the entire process thus the following condition holds,

$$g^B = -\mathbf{u}^B \cdot \mathbf{n} - \delta = -\left(\mathbf{u} - \frac{1}{2}\ell\ (\mathbf{S} - \mathbf{N})\,\psi\right) \cdot \mathbf{n} - \delta = -\left(u_2 + \frac{1}{2}\ell\,(1 - \psi_0)\,\psi\right) - \delta = 0. \tag{42}$$

At the same time, point A is initially in separation and it may come into contact during the process, thus

$$g^A = \ell\psi_0 - \mathbf{u}^A \cdot \mathbf{n} - \delta = \ell\psi_0 - \delta - \left(\mathbf{u} - \frac{1}{2}\ell\ (\mathbf{S} + \mathbf{N})\,\psi\right) \cdot \mathbf{n} = \ell\psi_0 - \delta - \left(u_2 - \frac{1}{2}\ell\ (1 + \psi_0)\,\psi\right) \geq 0. \tag{43}$$

The strong form of the equilibrium system (19) combined with the constitutive equations (16) simplifies to the following set of differential equations,

$$\begin{cases} \beta\psi' + u_1'' = 0, \\ \left(1 - \frac{1}{2}\beta\right)\left(\ell^2\psi'' + u_1'\right) - \beta\psi - u_1' = 0, \\ u_2'' = 0, \end{cases} \tag{44}$$

where the prime denotes differentiation with respect to x_2 and $\beta = 2\eta/(1+\eta)$, where $\eta = \mu_c/\mu$. For $\eta = 0$, which corresponds to $\beta = 0$, a set of three harmonic and decoupled equations for u_1, u_2 and ψ is obtained.

Consider first the case of partial contact, $g^A > 0$. Utilizing the contact model and the symmetry of the problem with respect to $x_2 = 0$, the boundary conditions are then as follows,

$$\begin{aligned} &u_1(0) = 0, \qquad u_2(0) = 0, \qquad m_2(0) = 0, \\ &\sigma_{12}(H) = 0, \qquad g^B(H) = 0, \qquad m_2(H) = \tfrac{1}{2}\ell(1-\psi_0)\sigma_{22}(H). \end{aligned} \tag{45}$$

The condition for the micromoment at $x_2 = H$ results from Eq. (29). With the normal $\mathbf{n}$ aligned with $\mathbf{e}_2$, the contact traction t_n is equal to σ_{22}, and the effective moment lever acting with respect to the centroid of the microblock equals $\frac{1}{2}\ell(1-\psi_0)$. These conditions hold true as long as the microrotation at the surface does not exceed the initial microrotation ψ_0. Then, with further compression, we have $g^A = 0$ and, instead of the Neumann boundary condition on $m_2(H)$, the Dirichlet boundary condition $\psi(H) = -\psi_0$ becomes active.

The solution can be found in closed form and comprises two cases depending on the displacement δ applied to the rigid surface, viz.

$$\begin{aligned} u_1(x_2) &= \begin{cases} \ell\sqrt{\beta}A_1 \sinh\left(\dfrac{x_2\sqrt{\beta}}{\ell}\right) & \text{for } \delta < \delta_{fc}, \\ \ell\sqrt{\beta}A_2 \sinh\left(\dfrac{x_2\sqrt{\beta}}{\ell}\right) & \text{for } \delta \geq \delta_{fc}, \end{cases} \\ \psi(x_2) &= \begin{cases} -A_1 \cosh\left(\dfrac{x_2\sqrt{\beta}}{\ell}\right) & \text{for } \delta < \delta_{fc}, \\ -A_2 \cosh\left(\dfrac{x_2\sqrt{\beta}}{\ell}\right) & \text{for } \delta \geq \delta_{fc}, \end{cases} \\ u_2(x_2) &= \begin{cases} -4A_1 \dfrac{\sqrt{\beta}}{1-\psi_0}\dfrac{\mu}{\lambda+2\mu} \sinh\left(\dfrac{H\sqrt{\beta}}{\ell}\right)x_2 & \text{for } \delta < \delta_{fc}, \\ -\left(\delta - \dfrac{1}{2}\psi_0\ell(1-\psi_0)\right)\dfrac{x_2}{H} & \text{for } \delta \geq \delta_{fc}, \end{cases} \end{aligned} \tag{46}$$

with A_1, A_2 and δ_{fc} defined as

$$\begin{aligned} A_1 &= \frac{2(\lambda+2\mu)(1-\psi_0)\delta}{\ell(\lambda+2\mu)(1-\psi_0)^2\cosh\left(\frac{H\sqrt{\beta}}{\ell}\right) + 8H\sqrt{\beta}\mu\sinh\left(\frac{H\sqrt{\beta}}{\ell}\right)}, \\ A_2 &= \psi_0 \operatorname{sech}\left(\frac{H\sqrt{\beta}}{\ell}\right), \\ \delta_{fc} &= \frac{1}{2}\psi_0\left(\ell(1-\psi_0) + \frac{8H\sqrt{\beta}\mu\tanh\left(\frac{H\sqrt{\beta}}{\ell}\right)}{(\lambda+2\mu)(1-\psi_0)}\right), \end{aligned} \tag{47}$$

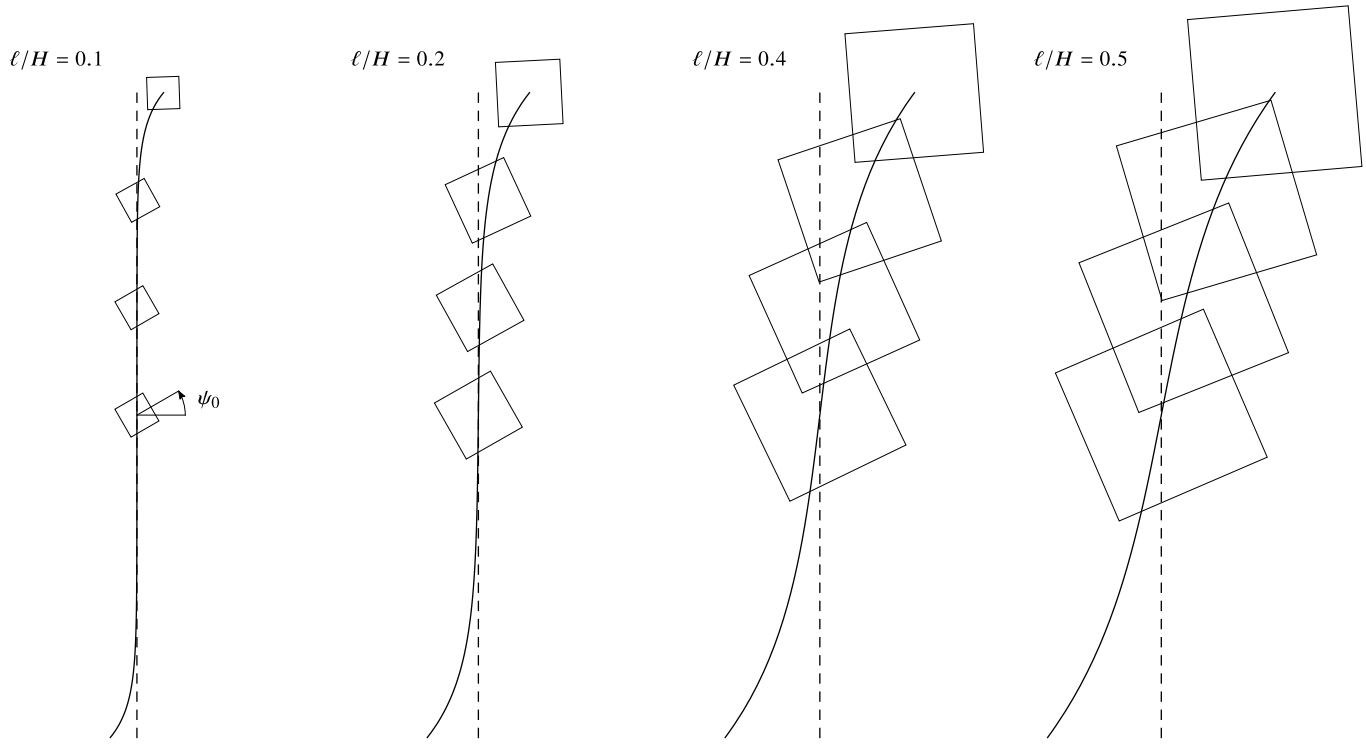

Figure 3: Boundary layers induced by contact conditions in the infinite strip compressed by two rigid planes. The solid lines illustrate the horizontal displacement u_1 magnified 25 times (the vertical displacement u_2 is not shown). The squares illustrate the microrotation ψ with respect to the initial microrotation ψ_0 prescribed at the contact surface; the rotations are magnified 30 times.

where δ_{fc} denotes the value of δ when the gap at corner A closes and full contact is achieved. In addition to the strip thickness H and initial microrotation ψ_0, the solution depends on the parameters β and ℓ that characterize the isotropic elastic Cosserat material in 2D and on Poisson's ratio ν (through Lamé's constants λ and μ).

The deformation pattern is shown in Fig. 3 for selected values of the strip thickness characterized by the ratio ℓ/H. Unless otherwise specified, the results shown in Fig. 3 and in the subsequent figures correspond to $\psi_0 = 1°$, $\nu = 0.3$, $\beta = 1$ (so that $\eta = 1$), and $\delta = 0.02H$. In Fig. 3, the horizontal displacement u_1 is depicted as the deviation of the solid lines from the vertical dashed lines that correspond to the initial state. The squares of the side length ℓ illustrate the microrotation ψ at four positions between $x_2 = 0$ and $x_2 = H$. Each square is rotated counterclockwise by the angle $\psi_0 + \psi$, where $\psi_0 = 1°$ and ψ is negative (for better visibility, the rotation angle has been magnified 30 times). The vertical displacement u_2 is linear in x_2, thus it is not shown.

The diagrams of the microrotation ψ and displacement u_1 are shown in Fig. 4. The markers depict the finite-element solution which shows a perfect agreement with the analytical solution represented by the solid lines. The finite-element solution has been obtained using 20 solid elements per strip half-thickness; for the sake of clarity, the markers are shown for every second node.

For a thick strip, see e.g. the case of $\ell/H = 0.1$ in Figs. 3 and 4, the solution exhibits boundary layers induced by the contact conditions, and specifically by the contact micromoments that are coupled to the contact traction through the microblock model. The resulting microrotation ψ and horizontal displacement u_1 decay exponentially

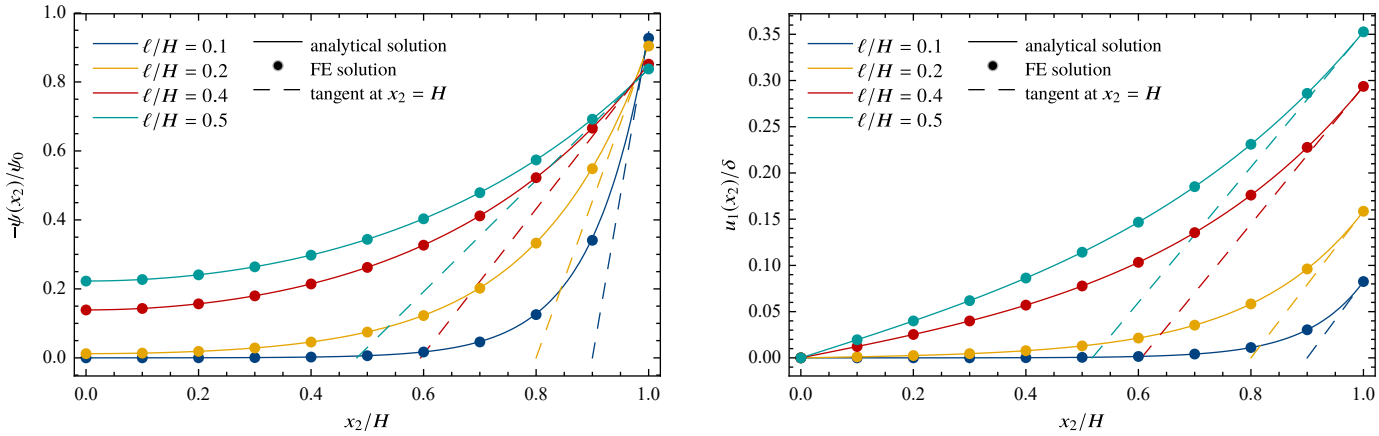

(a) (b)

Figure 4: Infinite strip compressed by two rigid planes: (a) microrotation ψ normalized by $-\psi_0$ and (b) displacement u_1 normalized by $\delta = 0.02H$. The solid lines and the markers indicate the analytical solution and the finite-element solution, respectively.

with the distance from the contact surface and ultimately vanish in the bulk of the strip. In a twice thinner strip, for $\ell/H = 0.2$, the boundary layers occupy almost the entire strip thickness, and for even thinner strips the region of vanishing ψ and u_1 does not occur.

The thickness of the boundary layer can be represented by a characteristic length obtained by dividing the value of the field at the surface by the spatial derivative of the field with a minus sign, thus

$$L_\psi = -\frac{\psi(H)}{\psi'(H)}, \qquad L_u = -\frac{u_1(H)}{u_1'(H)}. \tag{48}$$

In Fig. 4, the characteristic lengths L_ψ and L_u correspond to the distance from the point of $x_2/H = 1$ to the point of intersection of the respective dashed line with the horizontal axis $\psi = 0$ or $u_1 = 0$. Interestingly, it turns out that the characteristic lengths L_ψ and L_u do not depend on the solution branch corresponding the partial or full contact, and have a particularly simple closed-form representation upon introducing the normalization by $\ell/\sqrt{\beta}$,

$$\frac{\sqrt{\beta}L_\psi}{\ell} = \coth\left(\frac{\sqrt{\beta}H}{\ell}\right), \qquad \frac{\sqrt{\beta}L_u}{\ell} = \tanh\left(\frac{\sqrt{\beta}H}{\ell}\right). \tag{49}$$

Fig. 5 shows the dependence of the normalized characteristic lengths on the normalized strip thickness $\sqrt{\beta}H/\ell$. It follows that, for relatively thick strips, the normalized lengths $\sqrt{\beta}L_\psi/\ell$ and $\sqrt{\beta}L_u/\ell$ are equal one to the other (and equal to unity). This regime corresponds to the fully developed boundary layers exhibiting an exponential decay towards the strip bulk. As the normalized strip thickness decreases, the normalized characteristic lengths start to deviate one from the other ($\sqrt{\beta}L_\psi/\ell$ increases and $\sqrt{\beta}L_u/\ell$ decreases), which corresponds to the situation when the boundary layers occupy the entire strip thickness.

Finally, let us discuss the boundary conditions resulting from the microblock contact model. Fig. 6a shows the evolution of the micromoment M at the contact interface for $\ell/H = 0.5$. Here, the micromoment M is normalized by the micromoment $M(\delta_{\mathrm{fc}})$ at the instant of transition from the partial contact to the full contact, i.e. for $\delta = \delta_{\mathrm{fc}}$ (solid line), and by the contact traction t_{n} multiplied by $\frac{1}{2}\ell(1-\psi_0)$, so that it corresponds to the

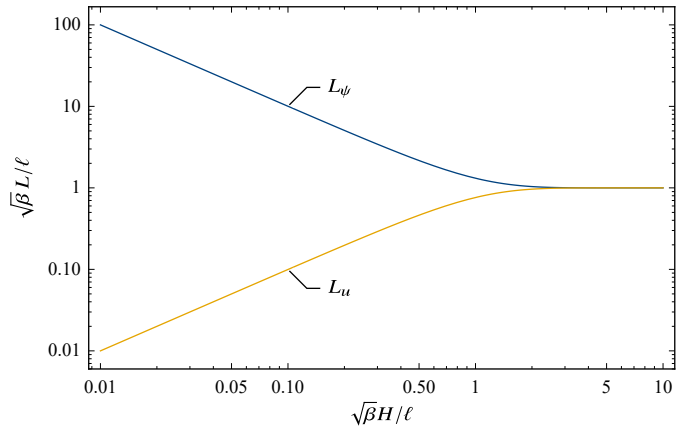

Figure 5: Dependence of the boundary layer thickness represented by the normalized characteristic lengths $\sqrt{\beta}L_\psi/\ell$ and $\sqrt{\beta}L_u/\ell$ on the normalized strip thickness $\sqrt{\beta}H/\ell$, cf. Eq. (49).

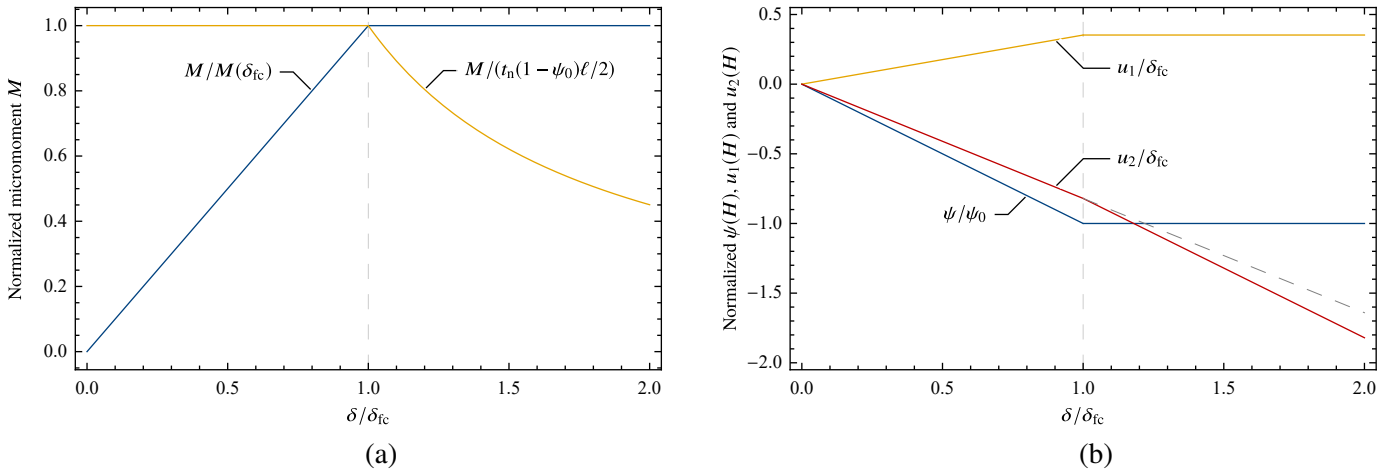

Figure 6: Infinite strip compressed by two rigid planes: evolution of micromoment M (a) and microrotation and displacement (b) at the contact interface.

effective moment lever (dashed line). During the first stage of compression when partial contact persists, i.e. for $\delta < \delta_{\rm fc}$, the micromoment M increases linearly as it is then proportional to the contact traction $t_{\rm n}$. At the same time, the effective moment lever is then constant and equal to $\frac{1}{2}\ell(1-\psi_0) \approx \frac{1}{2}\ell$, since contact traction is applied at one corner only. During the second stage when full contact occurs, i.e. for $\delta > \delta_{\rm fc}$, the micromoment M is constant and equal to the value at the instant of $\delta = \delta_{\rm fc}$. The effective moment lever then decreases since the contact traction is applied to both corners, $t_{\rm n} = t_{\rm n}^A + t_{\rm n}^B$, while the micromoment depends on the difference between the two components, $M = \frac{1}{2}\ell(t_{\rm n}^B - t_{\rm n}^A)(1-\psi_0)$, which is constant.

The corresponding evolution of the microrotation $\psi(H)$ and displacement components $u_i(H)$ at the contact nterface is shown in Fig. 6b. During the first stage, the microrotation $\psi(H)$ linearly increases in absolute value note that $\psi(H)$ is negative) until it reaches the value of $-\psi_0$ at the instant of transition to the full contact, and ubsequently it is constant. Likewise, the horizontal displacement $u_1(H)$ is proportional to δ during the first stage, nd then it is constant. The dependence of the vertical displacement $u_2(H)$ on δ is piecewise-linear with a change

of the slope at the instant of transition from partial to full contact.

To conclude this subsection, let us note that nontrivial effects are introduced by non-standard boundary conditions, here resulting from the microblock contact model. In particular, boundary layers are introduced of the thickness related to the length-scale parameter ℓ of the Cosserat material, and an analytical solution has been derived for the simple problem of an infinite strip with nonaligned microblocks compressed by two rigid planes. In the next subsection, a more complex Hertz-like contact problem is solved numerically.

4.2 Hertz-like contact problem

In this section, a problem similar to the classic Hertz contact problem is analyzed in the 2D setting, namely contact between a Cosserat elastic half-plane and a rigid cylinder of radius R loaded by force P, cf. Fig. 7a. At the contact interface, the microblock contact model of Section 3 is employed and, as a reference, also the classic unilateral contact model in which the usual impenetrability condition is accompanied by the condition of vanishing micromoment, $M = 0$.

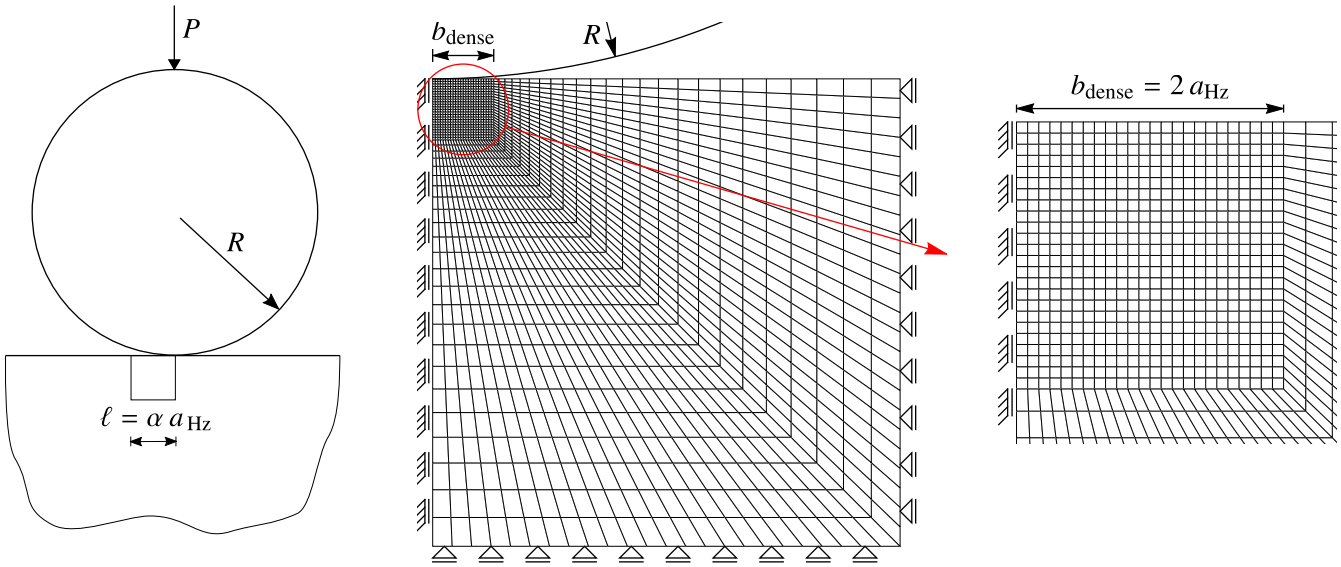

Figure 7: Hertz-like contact problem for a Cosserat elastic half-space: (a) scheme of the 2D problem, (b) finite-element mesh, (c) magnification of the refined mesh region. The actual mesh used in the computations is five times finer, i.e. each element shown in the figure is divided into $5 \times 5 = 25$ elements.

The finite element mesh used in the computations is illustrated in Fig. 7b. Note that a coarse mesh is shown in Fig. 7b for better visibility, while the actual mesh was five times finer with the total number of unknowns of about 130 000. In the vicinity of the contact zone, a regular and dense mesh region of the size of $2a_{\mathrm{Hz}}$ is used, cf. Fig. 7c, where a_{Hz} is the contact half-width in the classic Hertz solution at $P = P_{\max}$,

$$a_{\mathrm{Hz}} = \sqrt{\frac{4P_{\max}R}{\pi E^*}}, \qquad p_{\mathrm{Hz}} = \frac{2P_{\max}}{\pi a_{\mathrm{Hz}}}, \qquad E^* = \frac{E}{1-\nu^2}, \tag{50}$$

and the maximum Hertzian contact pressure p_{Hz} is also provided above for future reference. The symmetry of

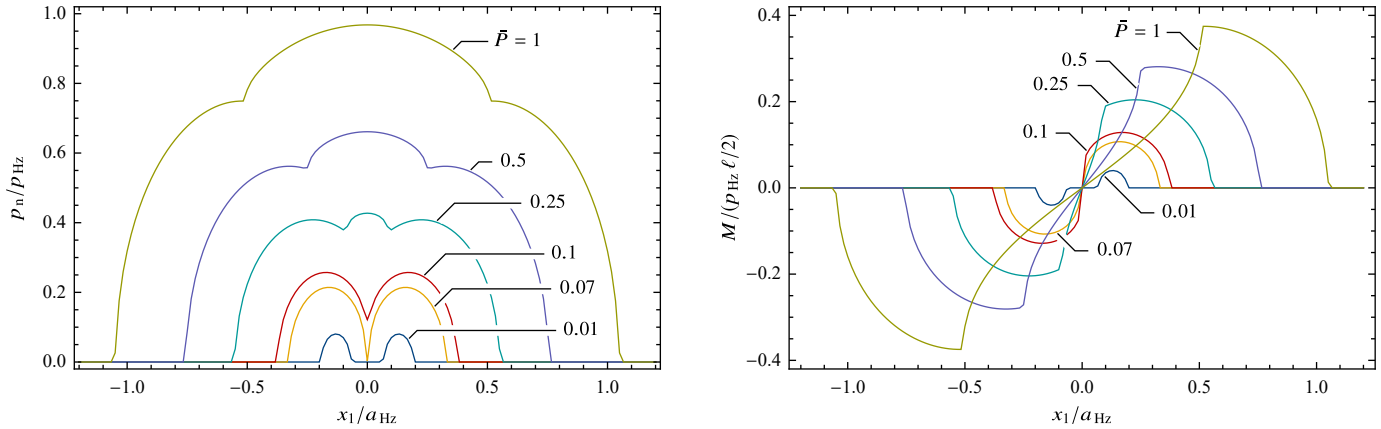

Figure 8: Hertz-like contact problem: (a) normalized contact pressure p_n and (b) normalized micromoment M as a function of the normalized load $\bar{P} = P/P_{max}$ for $\alpha = 0.25$.

the problem is utilized, so that the problem is formulated for one half of the half-space. The boundary conditions on the symmetry axis, $x_1 = 0$, apart from the classic counterpart $u_1 = 0$, include also the constraint on the microrotation, $\psi = 0$. Upon truncation, the corresponding computational domain is a square of the size of $18a_{Hz}$.

The evolution of the *contact pressure* $p_n = -t_n$ and micromoment M, both normalized using the Hertzian contact pressure p_{Hz}, is shown in Fig. 8 for selected stages of indentation characterized by the normalized load $\bar{P} = P/P_{max}$. Here and below, the results are shown in a dimensionless form, and they depend only on two material parameters, $\nu = 0.3$ and $\beta = 1$, and on parameter $\alpha = \ell/a_{Hz}$ that relates the length scale parameter ℓ to the Hertz contact size a_{Hz}. Parameter α governs thus the size effects. Considering that a_{Hz} depends on the load P_{max}, parameter α can also be interpreted as the parameter specifying the load. Indeed, for fixed material parameters, the higher the load P_{max}, the higher the contact size a_{Hz}, and thus the lower the parameter α. The results shown in Fig. 8 correspond to $\alpha = 0.25$. The actual computations are carried out for $E = 100$, $R = 10$ and $P = 1$ (with adequate physical units).

At the beginning of the indentation process, for $\bar{P} < 0.07$, contact occurs in two separated zones of partial contact (only one microblock corner is in contact in each zone). As the load increases, the two zones of partial contact grow and ultimately coalesce at $\bar{P} \approx 0.07$. Subsequently, the zone of full contact forms in the central part surrounded by two zones of partial contact. The distribution of the contact pressure exhibits a kink at the points of transition between the zones of full and partial contact, see Fig. 8a. The kinks are also visible in Fig. 8b showing the corresponding distributions of the micromoment M. Recall that the micromoment M results from the microblock model and is coupled to the local contact pressure p_n. The change of the interaction mode at the transition points between full and partial contact is associated with an abrupt change of the contact stiffness (both normal and micromoment stiffness). This leads to discontinuities of the slope of contact pressure and micromoment, i.e. the kinks visible in Fig. 8.

Consider now the case of the interface with nonaligned blocks, as in Section 4.1. The symmetry of the problem is, then, broken, and the problem is formulated for the complete half-space. The computations are thus carried out for a rectangular domain of the size $36a_{Hz} \times 18a_{Hz}$. The results shown in Fig. 9 correspond to the initial

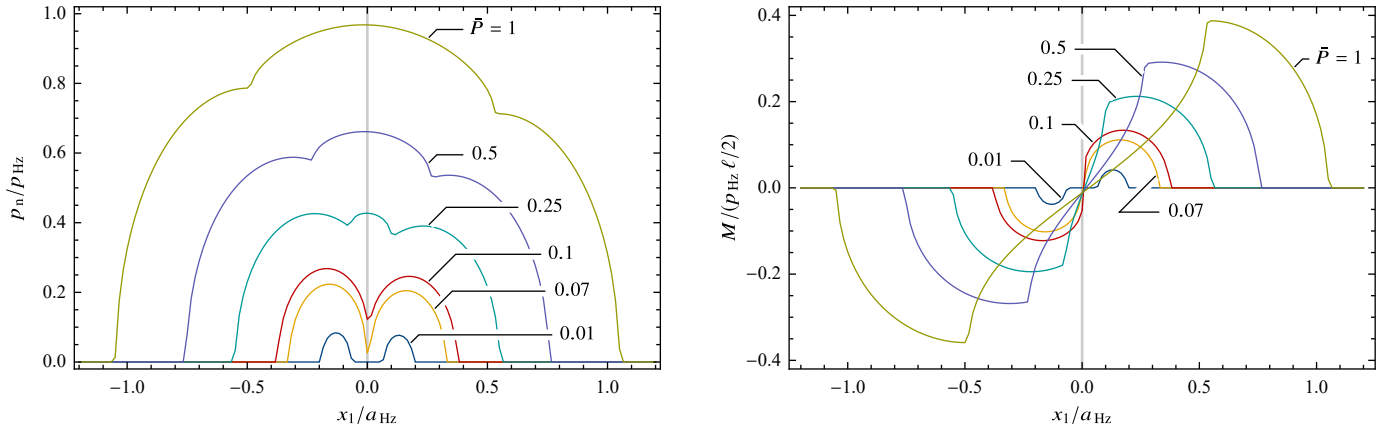

Figure 9: Hertz-like contact problem in the case of nonaligned microblocks with $\psi_0 = 5°$: (a) normalized contact pressure p_n and (b) normalized micromoment M as a function of the normalized load $\bar{P} = P/P_{max}$ for $\alpha = 0.25$.

counterclockwise misalignment angle $\psi_0 = 5°$. Specifically, the contact pressure p_n and the micromoment M are shown for the same values of the normalized load $\bar{P}$ as in the previous case. As expected, the solution is no longer symmetric with respect to $x_1 = 0$. However, the features, such as existence of the zones of separation and full or partial contact, are preserved. It can also be seen that the initial counterclockwise rotation leads to higher contact pressures for $x_1 < 0$ than for $x_1 > 0$. It is less apparent, but can also be observed, that the points of transition between the zones of full and partial contact are shifted to higher x_1, i.e. to the right in Fig. 9.

It can be seen in Figs. 8 and 9 that the qualitative features of the solution significantly depend on the load. The related changes in the solution are a manifestation of the size effects. Indeed, the actual contact width, which is a characteristic length scale of the problem, depends on the load, and so does the ratio of the material length scale ℓ to the actual contact width. Let us thus study in more detail the size effects introduced by the microblock contact model. Note that the Cosserat model involves the length scale parameter ℓ, hence the continuum model itself is expected to deliver size-dependent response also in the case of the classic unilateral contact model. The respective results will be used as a reference. Below, the size effects are analyzed by varying the internal length scale ℓ of the Cosserat continuum, while the load P_{max} is fixed. Specifically, the internal length scale ℓ is taken as a fraction α of the Hertz contact half-width a_{Hz} and α is varied.

Figure 10 shows the normalized contact pressure for α varied between 0.01 and 1.25 for both the microblock contact model and for the classic unilateral contact model. In order to improve the accuracy of the finite-element computations, in particular, to enable numerically exact determination of the actual contact area, the results reported in Fig. 10 have been obtained using a modified approach for the treatment of the contact constraints. Specifically, the positions of the nodes on the contact interface have been adjusted in an iterative manner such that the finite-element discretization matches the boundary of the contact zone. For relatively small α, the contact zone is simply connected, and the contact half-width a is to be found such that the conditions $g^A = 0$ and $p^A = 0$ hold simultaneously at the contact zone boundary at $x_1 = a$. For relatively large α, a separation zone occurs in the middle of the contact zone, and the positions of the two boundaries $x_1 = a$ (outer boundary) and $x_1 = b$ (inner boundary) are to be found such that the conditions $g^A = 0$ and $p_n^A = 0$ are simultaneously satisfied at

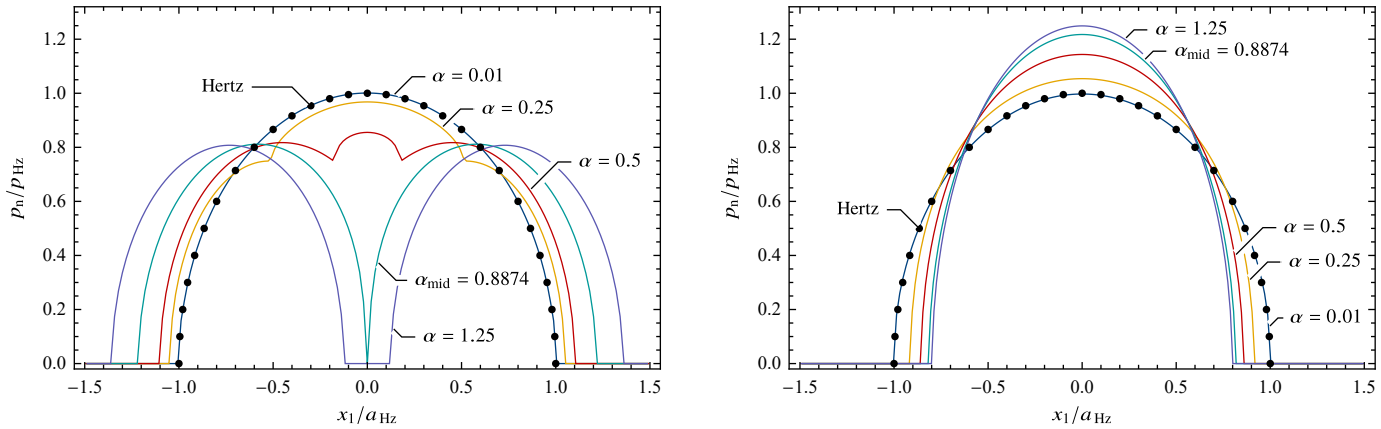

Figure 10: Size effects in the Hertz-like contact problem: effect of parameter $\alpha = \ell/a_{\mathrm{Hz}}$ on the normalized contact pressure p_{n} for the microblock contact model (a) and for the classic unilateral contact model (b).

both boundaries. Finally, in the intermediate case when the two contact zones coalesce, we have $g^A = 0$ and $p_{\mathrm{n}}^A = 0$ at $x_1 = a$ and on the symmetry axis $x_1 = 0$. Now, in addition to the contact half-width a, unknown is the corresponding value of parameter α, denoted by α_{mid}, that has been found equal to $\alpha_{\mathrm{mid}} = 0.8874$. In the case of the classic unilateral contact, the contact zone is simply connected and only the contact half-width a is found by following the procedure described above.

It can be seen in Fig. 10 that significant size effects are obtained for both contact models. In the size-independent limit of $\alpha \to 0$, see the case of $\alpha = 0.01$, the solution converges for both contact models to the solution of the classic Hertz contact problem (the respective contact pressure is indicated by markers in Fig. 10). In the case of the unilateral contact model, the distribution of contact pressure resembles the elliptic profile of the classic Hertz contact problem. However, with increasing α, the maximum contact pressure increases, while the contact width decreases. Accordingly, the hardness, defined as the average contact pressure, $H = P_{\max}/(2a)$, increases with respect to the hardness in the size-independent limit, denoted by H_{Hz}, as shown in Fig. 11a.

In the case of the microblock contact model, the contact half-width a increases with increasing α. This is accompanied by significant changes of the contact pressure profile, as already shown in Fig. 8a. Interestingly, in a wide range of values of α, say for $\alpha > 0.5$, the maximum contact pressure is approximately constant. Since the contact width increases, the hardness decreases with increasing α, cf. Fig. 11a. However, considering that two contact zones are formed at high values of α, the hardness can be determined in two ways. The apparent hardness is obtained by dividing the load $P_{\max}$ by the contact width $2a$, and the apparent hardness decreases monotonically with increasing α. The real hardness is obtained by dividing the load $P_{\max}$ by the real contact area $2(a - b)$, where b is the half-width of the separation zone in the middle of the contact zone. The real hardness corresponds thus to the average contact pressure in the actual contact zones. The dependence of the real hardness on α is not monotonic, as it increases with increasing α for $\alpha > \alpha_{\mathrm{mid}}$, and in this range the real hardness deviates from the apparent one, see the inset in Fig. 8a.

The size effect on hardness observed for the elastic Cosserat continuum in the case of the classic unilateral contact condition follows the usual trend, namely the hardness increases with decreasing size of the contact zone.

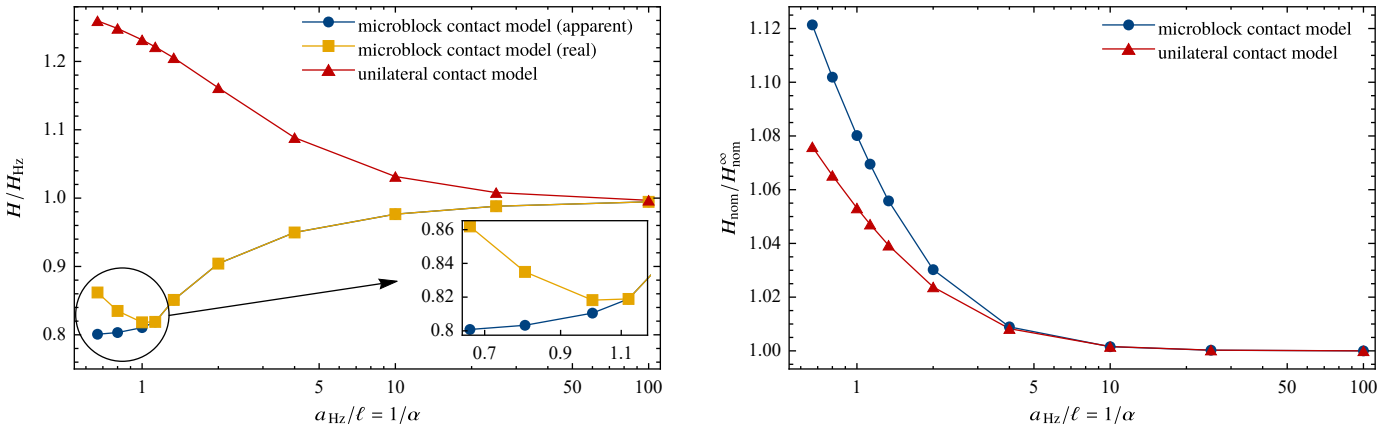

Figure 11: Size effects in the Hertz-like contact problem: (a) normalized hardness H/H_{Hz} and (b) normalized nominal hardness $H_{\mathrm{nom}}/H^{\infty}_{\mathrm{nom}}$ as a function of $1/\alpha$.

Equivalently, the hardness increases with increasing material length scale parameter ℓ, while the load and the indenter radius are fixed. In the case of the microblock contact model, the effect is opposite—hardness decreases with increasing material length-scale parameter ℓ—with a non-trivial non-monotonic behavior observed in terms of the real hardness at small scale when the length scale ℓ approaches the size of the contact zone.

Figure 11b illustrates the size effects in terms of the nominal hardness $H_{\mathrm{nom}} = P_{\max}/(2a_{\mathrm{nom}})$, where $a_{\mathrm{nom}} = \sqrt{d(2R-d)}$ is the nominal contact width that is obtained from purely geometrical considerations, and H_{nom} is normalized by $H^{\infty}_{\mathrm{nom}}$, i.e. the hardness corresponding to $1/\alpha \to \infty$. For both contact models, the nominal hardness increases with increasing α. Accordingly, the overall stiffness increases with increasing α, and the effect is more pronounced for the microblock contact model. In the case of the unilateral contact model, the increase of stiffness results from the additional energy terms in the Cosserat continuum that are related to the rotations and curvature gradients, and these terms exhibit the usual size dependence, i.e. they increase with decreasing scale. In the case of the microblock model, additional stiffening is introduced by the contact model itself. Note that, in the full contact zone, contact interaction enforces a non-zero microrotation that would be relaxed if the condition $M = 0$ was imposed, as in the unilateral contact model. This is associated with some elastic strain energy stored in the subsurface layer. This contributes to the overall stiffness and to an additional increase of the nominal hardness.

Let us examine the subsurface layers in more detail. From Fig. 10 it follows that, for both contact models, the solution converges to the classic Hertz solution when α tends to zero, see e.g. the case of $\alpha = 0.01$. However, the boundary conditions related to the microrotation are different in the two models. In the case of the unilateral contact model, the boundary condition $M = 0$ is imposed on the micromoment, which implies that the normal derivative of the microrotation vanishes, i.e. $\partial\psi/\partial x_2 = 0$. On the contrary, a nonzero micromoment is imposed by the microblock contact model, and thus the normal derivative of ψ does not vanish at the contact surface. Accordingly, the two solutions must show some differences in terms of the microrotation ψ, and this is illustrated in Fig. 12a for $\alpha = 0.05$.

The difference between the two solutions is clearly visible in the vicinity of the surface, while far from the surface the difference vanishes. The respective difference of the two solutions, denoted by $\Delta\psi$, is shown in

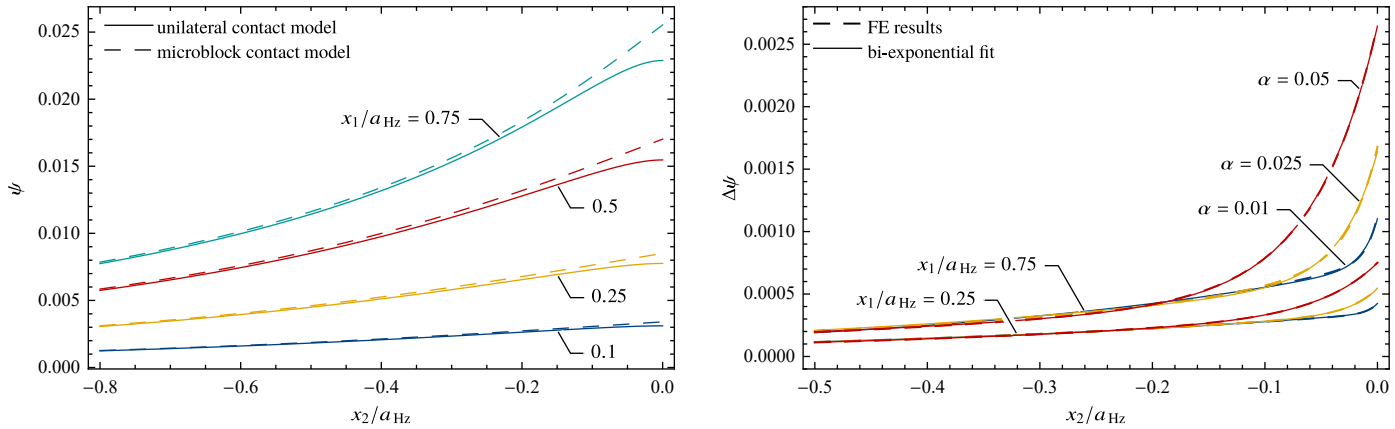

Figure 12: Effect of the contact model on the microrotation ψ in the subsurface layer: (a) dependence of the microrotation ψ on x_2/a_{Hz} for the two contact models and for $\alpha = 0.05$; (b) the respective difference $\Delta\psi$ and its fit by the bi-exponential decay function (51).

Fig. 12b at two representative positions x_1/a_{Hz} and for three values of α. It follows that the difference $\Delta\psi$ can be very well approximated by the following bi-exponential decay function,

$$\Delta\psi = A_{\mathrm{sol}} e^{x_2/L_{\mathrm{sol}}} + A_{\mathrm{bl}} e^{x_2/L_{\mathrm{bl}}}. \tag{51}$$

The first term describes the overall difference between the two solutions with A_{sol} and L_{sol} depending on x_1/a_{Hz} and weakly on α. The second term describes the boundary layer that is associated with the difference in the boundary conditions, as discussed above, and L_{bl} characterizes the thickness of the boundary layer with $L_{\mathrm{bl}} < L_{\mathrm{sol}}$. The dashed lines in Fig. 12b depict the bi-exponential function (51) fitted to the respective finite-element results. Note that the results reported in Fig. 12 (and in Fig. 13 below) have been obtained using a significantly refined finite-element mesh such that the element size in the vicinity of the surface is equal to $\ell/8$ in the case of the smallest characteristic length scale $\ell = 0.01 a_{\mathrm{Hz}}$ with the total number of unknowns reaching three million.

Figure 13 shows the boundary layer thickness parameter L_{bl} as a function of the position x_1/a_{Hz} along the contact interface. It turns out that the normalized thickness L_{bl}/ℓ is close to unity, except for $\alpha = 0.01$ in the range of x_1/a_{Hz} greater than, say, 0.7. Recall now the boundary layers studied in Section 4.1 and, in particular, Eq. $(49)_1$ for the characteristic length L_ψ. In the case of a thick strip, which is relevant here, we have $\sqrt{\beta} L_\psi/\ell = 1$, see Fig. 5. Considering that in the present computations parameter β has been assumed equal to unity, $\beta = 1$, it follows that $L_{\mathrm{bl}} \approx L_\psi$. This confirms that the difference in the solutions corresponding to the two contact models can indeed be interpreted in terms of the boundary layer induced by the difference in the boundary condition imposed on the microrotation ψ.

5 Conclusion

A microblock contact model has been derived for the Cosserat continuum based on micromechanical considerations. The goal has been to formulate, in a consistent manner, an enhanced contact model that introduces

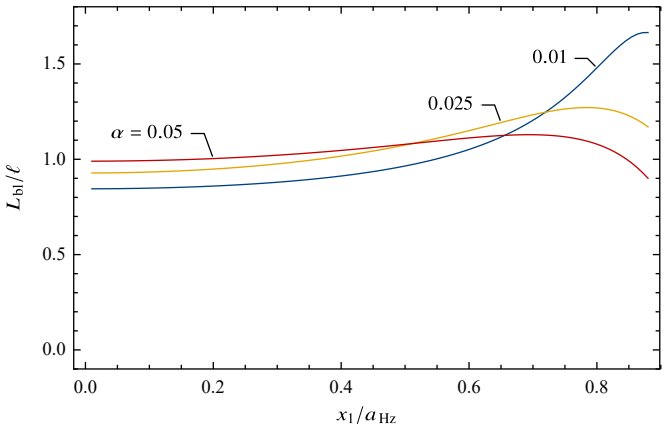

Figure 13: Dependence of the boundary layer thickness parameter L_{bl} on x_1/a_{Hz} and α.

non-standard contact conditions involving non-standard contact variables that are characteristic for a generalized continuum, like the Cosserat continuum. Specifically, the microrotation (generalized displacement) and the micromoment (generalized traction) at the contact surface are involved in the contact law in addition to the usual contact variables such as the normal gap and contact pressure. This is in contrast to the simplest assumption that the generalized tractions vanish on the contact surface, which is, in fact, a common choice in contact mechanics of generalized continua.

The physical interpretation of the microrotation, which is the additional degree of freedom in the Cosserat theory, and of the internal length-scale present in the theory has been exploited so that the model involves no additional material parameters. Even more importantly, the model exhibits a potential structure, which is a desired feature when the (hypothetical) underlying microstructured material is elastic. This is apparent in the case of the penalty regularization of the local impenetrability conditions, when the non-standard contact conditions derive from the penalty-regularized potential energy functional and can be easily shown to satisfy the resulting symmetry condition. This is less apparent, but still holds true, in the case of the augmented Lagrangian treatment of the local impenetrability conditions, which has been employed in the actual finite-element implementation.

Two illustrative contact problems have been solved to show the importance of the coupling between the standard (normal gap and contact pressure) and non-standard (microrotation and micromoment) contact variables. Firstly, an analytical solution has been found for the problem of compression of an infinite strip with initially misaligned blocks. The solution features boundary layers that are induced by the micromoments governed by the enhanced contact model. The analytical solution has been also used to validate the finite-element implementation. Secondly, a Hertz-like problem has been solved using the finite-element method. The respective solutions exhibit non-trivial features that are introduced by the microblock contact model. Furthermore, the Cosserat model, when combined with the classic unilateral contact model, exhibits the usual indentation size effect (hardness increases with decreasing indentation depth), while the dependence is opposite when the microblock contact model is adopted. Finally, it has been shown that boundary layers, similar to those observed in the infinite strip problem, develop beneath the indenter. Overall, it has been shown that consideration of the non-standard contact conditions may lead to new qualitative effects in contact mechanics of generalized continua, which is an area for further investigations.

Acknowledgement This work has been partially supported by the National Science Center (NCN) in Poland through Grant No. 2015/17/N/ST8/01113.

References

D. Addessi. A 2D Cosserat finite element based on a damage-plastic model for brittle materials. *Comput. Struct.*, 135:20–31, 2014.

P. Alart and A. Curnier. A mixed formulation for frictional contact problems prone to Newton like solution methods. *Comput. Methods Appl. Mech. Eng.*, 92:353–375, 1991.

S. Casolo. Macroscopic modelling of structured materials: relationship between orthotropic Cosserat continuum and rigid elements. *Int. J. Solids Struct.*, 43:475–496, 2006.

M. Cerrolaza, J. Sulem, and A. Elbied. A Cosserat non-linear finite element analysis software for blocky structures. *Adv. Eng. Software*, 30:69–83, 1999.

E. Cosserat and F. Cosserat. *Théorie des corps déformables*. A. Hermann et fils, 1909.

A. C. Eringen. Mechanics of micromorphic continua. In E. Kröner, editor, *Mechanics of Generalized Continua*, pages 18–35. Springer-Verlag, 1968.

S. Forest, P. Boubidi, and R. Sievert. Strain localization patterns at a crack tip in generalized single crystal plasticity. *Scr. Mater.*, 44:953–958, 2001.

H. Gao and Y. Huang. Taylor-based nonlocal theory of plasticity. *Int. J. Solids Struct.*, 38:2615–2637, 2001.

Y. F. Gao, B. C. Larson, J. H. Lee, L. Nicola, J. Z. Tischler, and G. M. Pharr. Lattice rotation patterns and strain gradient effects in face-centered-cubic single crystals under spherical indentation. *J. Appl. Mech.*, 82, 2015.

N. Garg, C.-S. Han, and F. Alisafaei. Length scale dependence in elastomers – comparison of indentation experiments with numerical simulations. *Polymers*, 98:201–209, 2016.

P. A. Gourgiotis, Th. Zisis, and K. P. Baxevanakis. Analysis of the tilted flat punch in couple-stress elasticity. *Int. J. Solids Struct.*, 85–86:34–43, 2016.

P. A. Gourgiotis, Th. Zisis, A. E. Giannakopoulos, and H. G. Georgiadis. The Hertz contact problem in couple-stress elasticity. *Int. J. Solids Struct.*, 168:228–237, 2019.

M. E. Gurtin. On the plasticity of single crystals: free energy, microforces, plastic-strain gradients. *J. Mech. Phys. Solids*, 48:989–1036, 2000.

. Hård af Segerstad, S. Toll, and R. Larsson. A micropolar theory for the finite elasticity of open-cell cellular solids. *Proc. R. Soc. A*, 465:843–865, 2009.

Y. Huang, Z. Xue, H. Gao, W. D. Nix, and Z. C. Xia. A study of microindentation hardness tests by mechanism-based strain gradient plasticity. *J. Mater. Res.*, 15:1786–1796, 2000.

Y. Huang, F. Zhang, K. C. Hwang, W. D. Nix, G. M. Pharr, and G. Feng. A model of size effects in nano-indentation. *J. Mech. Phys. Solids*, 54:1668–1686, 2006.

W. T. Koiter. Couple stresses in the theory of elasticity: I & II. *Proc. K. Ned. Akad. Wet. (B)*, 67:17–44, 1964.

J. Korelc. Automation of primal and sensitivity analysis of transient coupled problems. *Comput. Mech.*, 44: 631–649, 2009.

J. Korelc and P. Wriggers. *Automation of Finite Element Methods*. Springer, 2016.

R. Lakes. On the torsional properties of single osteons. *J. Biomech.*, 28:1409–1409, 1995.

W. B. Lee and Y. P. Chen. Simulation of micro-indentation hardness of FCC single crystals by mechanism-based strain gradient crystal plasticity. *Int. J. Plast.*, 26:1527–1540, 2010.

J. Lengiewicz, J. Korelc, and S. Stupkiewicz. Automation of finite element formulations for large deformation contact problems. *Int. J. Numer. Methods Eng.*, 85:1252–1279, 2011.

M. J. Lewandowski and S. Stupkiewicz. Size effects in wedge indentation predicted by a gradient-enhanced crystal-plasticity model. *Int. J. Plast.*, 109:54–78, 2018.

P. Li and T.-J. Liu. The two-dimensional adhesive contact problem in the theory of couple stress elasticity. *J. Adhes. Sci. Technol.*, 2019. doi: 10.1080/01694243.2019.1693168.

X. N. Liu, G. L. Huang, and G. K. Hu. Chiral effect in plane isotropic micropolar elasticity and its application to chiral lattices. *J. Mech. Phys. Solids*, 60:1907–1921, 2012.

R. Masiani, N. Rizzi, and P. Trovalusci. Masonry as structured continuum. *Meccanica*, 30:673–683, 1995.

R. D. Mindlin. Second gradient of strain and surface-tension in linear elasticity. *Int. J. Solids Struct.*, 1:417–438, 1965.

R. D. Mindlin and H. F. Tiersten. Effects of couple-stresses in linear elasticity. *Arch. Ration. Mech. Anal.*, 11: 415–448, 1962.

H.-B. Mühlhaus and E. C. Alfantis. A variational principle for gradient plasticity. *Int. J. Solids Struct.*, 28: 845–857, 1991.

. Nakamura and R. S. Lakes. Finite element analysis of stress concentration around a blunt crack in a Cosserat elastic solid. *Comput. Methods Appl. Mech. Eng.*, 66:257–266, 1988.

. Neff. Relations of constants for isotropic linear Cosserat elasticity. Technical report, Fachbereich Mathematik, Technische Universität Darmstadt, 2008.

P. Neff, J. Jeong, and A. Fischle. Stable identification of linear isotropic cosserat parameters: bounded stiffness in bending and torsion implies conformal invariance of curvature. *Acta Mech.*, 211:237–249, 2010.

W. D. Nix and H. Gao. Indentation size effects in crystalline materials: a law for strain gradient plasticity. *J. Mech. Phys. Solids*, 46:411–425, 1998.

J. Nocedal and S. Wright. *Numerical optimization*. Springer Science & Business Media, 2006.

W. Nowacki. *Theory of Micropolar Elasticity*. Springer, 1972.

G. M. Pharr, E. G. Herbert, and Y. Gao. The indentation size effect: a critical examination of experimental observations and mechanistic interpretations. *Annu. Rev. Mater. Res.*, 40:271–292, 2010.

S. Qu, Y. Huang, G. M. Pharr, and K. C. Hwang. The indentation size effect in the spherical indentation of iridium: A study via the conventional theory of mechanism-based strain gradient plasticity. *Int. J. Plast.*, 22: 1265–1286, 2006.

C. Reuber, P. Eisenlohr, F. Roters, and D. Raabe. Dislocation density distribution around an indent in single-crystalline nickel: Comparing nonlocal crystal plasticity finite-element predictions with experiments. *Acta Mater.*, 71:333–348, 2014.

J. Y. Shu and N. A. Fleck. The prediction of a size effect in microindentation. *Int. J. Solids Struct.*, 35:1363–1383, 1998.

H.-X. Song, L.-L. Ke, J. Su, J. Yang, K. Sritawat, and Y.-S. Wang. Surface effect on the contact problem of a piezoelectric half-plane. *Int. J. Solids Struct.*, 185-186:380–393, 2020.

A. Spadoni and M. Ruzzene. Elasto-static micropolar behavior of a chiral auxetic lattice. *J. Mech. Phys. Solids*, 60:156–171, 2012.

P. Steinmann. Theory and numerics of ductile micropolar elastoplastic damage. *Int. J. Numer. Methods Eng.*, 38: 583–606, 1995.

S. Stupkiewicz and H. Petryk. A minimal gradient-enhancement of the classical continuum theory of crystal plasticity. Part II: Size effects. *Arch. Mech.*, 68:487–513, 2016.

J. Sulem and H. B. Mühlhaus. A continuum model for periodic two-dimensional block structures. *Mech. of Cohesive-frict. Mater.*, 2:31–46, 1997.

S. Swaddiwudhipong, L. H. Poh, J. Hua, Z. S. Liu, and K. K. Tho. Modeling nano-indentation tests of glassy polymers using finite elements with strain gradient plasticity. *Mat. Sci. Eng. A*, 404:179–187, 2005.

. Tejchman. *Shear Localization in Granular Bodies with Micro-Polar Hypoplasticity*. Springer Science & Business Media, 2008.

J. Tejchman and E. Bauer. Numerical simulation of shear band formation with a polar hypoplastic model. *Comp. Geotech.*, 19:221–244, 1996.

I. Vardoulakis. Shear banding and liquefaction in granular materials on the basis of a Cosserat continuum theory. *Ingenieur Archiv.*, 59:106–113, 1989.

I. Vardoulakis. *Cosserat Continuum Mechanics: With Applications to Granular Media*. Springer International Publishing, 2019.

Y. Wang, H. Shen, X. Zhang, B. Zhang, J. Liu, and X. Li. Semi-analytical study of microscopic two-dimensional partial slip contact problem within the framework of couple stress elasticity: Cylindrical indenter. *Int. J. Solids Struct.*, 138:76–86, 2018.

Y. Wei and J. W. Hutchinson. Hardness trends in micron scale indentation. *J. Mech. Phys. Solids*, 51:2037–2056, 2003.

P. Wriggers. *Computational Contact Mechanics*. Springer Science & Business Media, 2006.

J. F. C. Yang and R. S. Lakes. Transient study of couple stress effects in compact bone: torsion. *J. Biomech. Eng.*, 103:275–279, 1981.

H. W. Zhang, H. Wang, P. Wriggers, and B. A. Schrefler. A finite element model for contact analysis of multiple Cosserat bodies. *Comput. Mech.*, 36:444–458, 2005.

Th. Zisis, P. A. Gourgiotis, K. P. Baxevanakis, and H. G. Georgiadis. Some basic contact problems in couple stress elasticity. *Int. J. Solids Struct.*, 51:2084–2095, 2014.